Global and Planetary Change 223 (2023) 104094

Contents lists available at ScienceDirect

Global and Planetary Change

journal homepage: www.elsevier.com/locate/gloplacha

Middle Jurassic terrestrial environmental and floral changes linked to volcanism: Evidence from the Qinghai-Tibet Plateau, China

Peixin Zhang [a,b,c], Minfang Yang [a], Jing Lu [b,*], Zhongfeng Jiang [c], Kai Zhou [d], Haoqing Liu [b], Zhen He [b], Ye Wang [b], Xiao Bian [b], Longyi Shao [b], Jason Hilton [e], David P.G. Bond [f,*]

[a] *Research Institute of Petroleum Exploration and Development, Petro China, Beijing 100083, PR China*
[b] *State Key Laboratory of Coal Resources and Safe Mining, College of Geoscience and Surveying Engineering, China University of Mining and Technology, Beijing 100083, PR China*
[c] *School of Municipal and Environmental Engineering, Henan University of Urban Construction, Pingdingshan, Henan 467036, PR China*
[d] *State Key Laboratory of Hydroscience and Engineering, Department of Hydraulic Engineering, Tsinghua University, Beijing 100084, PR China*
[e] *School of Geography, Earth and Environmental Sciences, The University of Birmingham, Edgbaston, Birmingham B15 2TT, UK*
[f] *School of Environmental Sciences, University of Hull, Hull HU6 7RX, UK*

ARTICLE INFO

Editor: Dr. Alan Haywood

Keywords:
Middle Jurassic
Terrestrial Qaidam Basin
Palynological fossils
Organic carbon isotope composition
Volcanism

ABSTRACT

The breakup of Pangaea and the rapid opening of the Ligurian and Central Atlantic oceans during the Middle Jurassic resulted in widespread volcanism accompanied by significant shifts in global environments, climates, and floras. Although major volcanism is a plausible driver of such global changes, linking these phenomena in the Middle Jurassic is hindered by a lack of detailed sedimentary records from which to evaluate cause and effect. Here, we link Middle Jurassic environmental, climatic, and floral changes with volcanism using records from the Dameigou section of the Qaidam Basin on the Qinghai-Tibet Plateau. High-resolution chemostratigraphic ($\delta^{13}C_{org}$ patterns) and biostratigraphic (palynological fossils) data reveal three negative organic carbon isotope excursions (NCIE) at the Aalenian-Bajocian boundary, the Bajocian-Bathonian boundary, and in the middle of the Callovian, respectively. The first two NCIEs (NCIE-I and NCIE-II) were accompanied by relatively warm and humid climatic conditions and coal accumulation. In contrast, the third NCIE (NCIE-III) was accompanied by warm but dry climatic conditions, a decrease in coal accumulation, a decline in plant diversity, the significant decline in fern spore diversity and abundance, and a rapid increase in the abundance of *Classopollis* pollen (based on petrological, palynological, PCA, Hydrophyte/Xerophyte ratio, and nMDS data). Four sedimentary mercury anomalies (Hg/Al_2O_3 spikes) have temporal coincidence with the three NCIEs and climate warming events, suggesting a volcanic origin for these. We suggest that volcanism was a key driver of Middle Jurassic change, with major pulses releasing large amounts of CO_2 and Hg into the atmosphere, resulting in Hg loading, NCIEs, climatic warming, and floral changes in terrestrial strata. Our multi-proxy study provides new insights into the links between volcanism and terrestrial environmental, climatic, and floral changes during the Middle Jurassic.

1. Introduction

The breakup of Pangaea and the rapid opening of the Ligurian and Central Atlantic oceans during the Middle Jurassic resulted in widespread volcanism and was accompanied by significant changes in global environments, climates, and floras (e.g., Jenkyns et al., 2002; Hesselbo et al., 2003; Dera et al., 2011; Deng et al., 2017; Al-Mojel et al., 2018). Strata from this interval record globally synchronous carbon isotope ($\delta^{13}C$) excursions that are associated with global warming and cooling events (Dera et al., 2011; Al-Mojel et al., 2018). Globally widespread positive carbon isotope excursions (PCIEs) are thought to be associated with ^{12}C-enriched organic matter (OM) sequestration in marine and terrestrial settings (Saltzman and Thomas, 2012). In contrast, negative carbon isotope excursions (NCIEs) have origins in the injection of large amounts of isotopically light carbon into the atmosphere-ocean system (e.g., Hesselbo et al., 2003; Al-Mojel et al., 2018). The source of this isotopically light carbon is controversial. Terrestrial OM oxidation, methane hydrate release, and large-scale volcanic activity are all considered potential sources of abundant light carbon (e.g., Hesselbo et al., 2003; Pellenard et al., 2014; Al-Mojel et al., 2018).

---

[*] Corresponding authors.
E-mail addresses: lujing@cumtb.edu.cn (J. Lu), d.bond@hull.ac.uk (D.P.G. Bond).

https://doi.org/10.1016/j.gloplacha.2023.104094
Received 2 December 2022; Received in revised form 10 March 2023; Accepted 17 March 2023

The role of volcanism in the global carbon cycle and environmental change has been widely recognized by previous studies, in which the direct input of gases to the atmosphere, and indirect contributions from magma intrusion into stored OM add a large amount of CO_2 and other products to the atmosphere (Svensen et al., 2009; Grasby et al., 2019; Shen et al., 2019, 2020; Lu et al., 2020a, 2020b, 2021a, 2021b; Zhang et al., 2022; Zhou et al., 2022). Volcanism is an important source of atmospheric Hg (Pyle and Mather, 2003), and it can be widely deposited in marine and terrestrial sediments after atmospheric transport (Sanei et al., 2012; Grasby et al., 2019, 2020; Shen et al., 2019, 2020, 2022a). Consequently sedimentary Hg enrichment has become an important proxy for major volcanism in the geological record (Sanei et al., 2012; Grasby et al., 2019, 2020; Shen et al., 2019, 2022a; Lu et al., 2020a, 2020b, 2021a, 2021b; Zhang et al., 2022; Zhou et al., 2022). Thus, mercury (Hg) geochemistry of sedimentary rocks can provide clues as to the source(s) of light carbon that contributes to NCIEs (e.g., Shen et al., 2019; Lu et al., 2021a). Intriguingly, sedimentary mercury anomalies are not reported in published studies for the Middle Jurassic, resulting in a lack of consensus around drivers for contemporaneous environmental changes.

Volcanism is considered a major driver of changes in plant communities and diversity during several key intervals during the Paleozoic and Mesozoic (e.g., Fielding et al., 2019; Mays et al., 2020; Wignall and Atkinson, 2020; Lindström, 2021; Lu et al., 2021a; Galasso et al., 2022; Marchetti et al., 2022; Zhang et al., 2022). Palynological material is widely distributed in sedimentary rocks and palynomorphs are easier to obtain in abundance than larger plant fossils (e.g., Litwin and Traverse, 1989; Wellman et al., 2003; Traverse, 2007; Wang et al., 2021). Based on the identification of the parent plants of palynological taxa and their adapted environments, palynological fossils have much potential for the reconstruction of paleo-vegetation and paleo-climatic features (e.g., Couper, 1958; Van Van Konijnenburg-Van Cittert, 1978; Du et al., 1982; Du, 1985; Balme, 1995; Wang et al., 1998, 2005; Wellman et al., 2003; Traverse, 2007; Rostovtseva, 2011; Deng et al., 2017; Lu et al., 2021a; Zhang et al., 2022). Numerous palynological studies of different regions, including the United Kingdom (Couper, 1958), Russia (Rostovtseva,

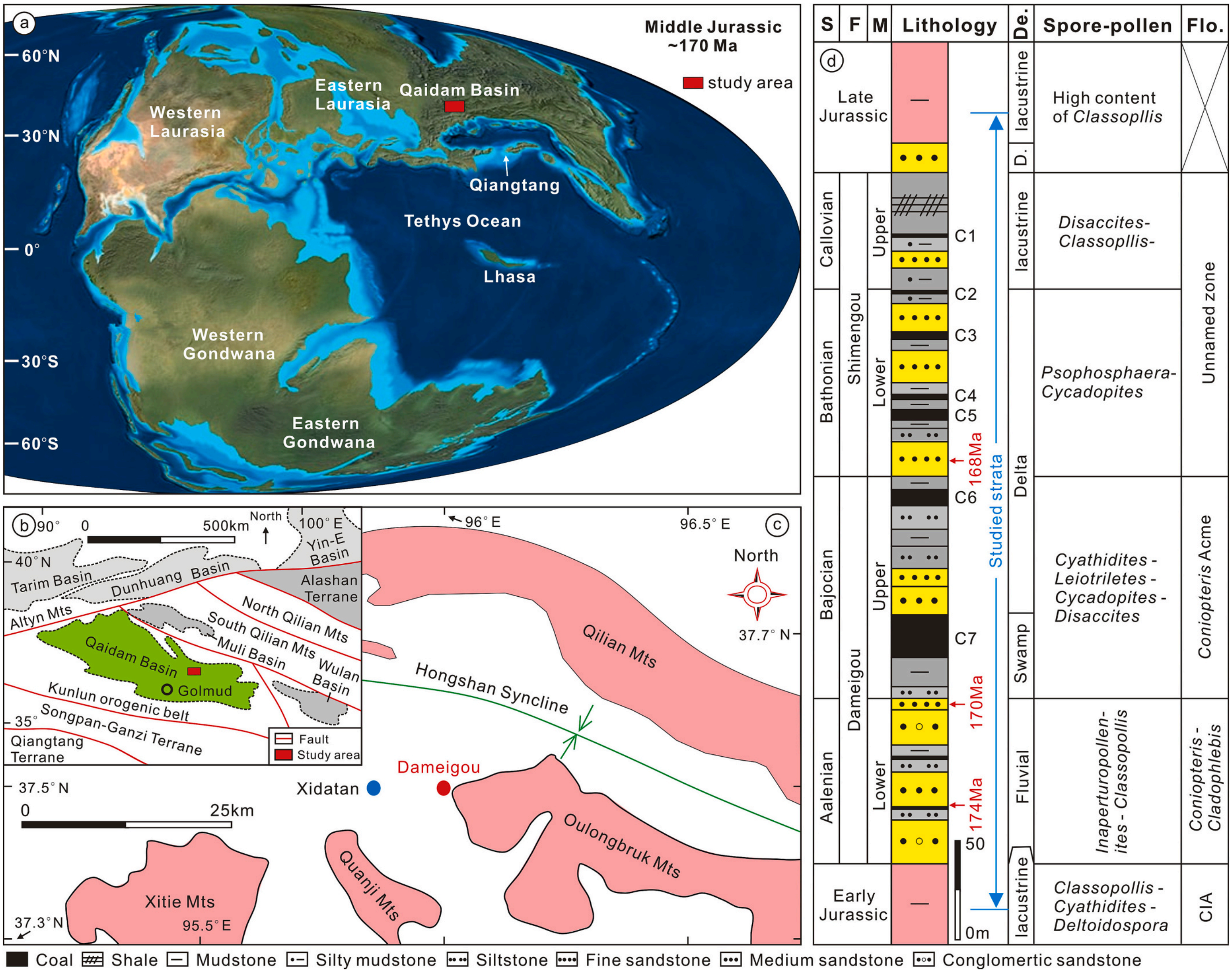

Fig. 1. Location and geological context for the study area. a, Paleogeographic reconstruction for the Middle Jurassic showing the location of the Qaidam Basin (modified from the ~170 Ma map of the webpage https://deeptimemaps.com/global-paleogeography-and-tectonics-in-deep-time); b, Tectonic setting for the Qaidam Basin and adjacent sedimentary basins (revised after Lu et al., 2016, 2018, 2020c); c, Enlargement from part e showing a sketch map with the location of the Dameigou Coalfield (revised after Lu et al., 2016, 2018, 2020c); d, Stratigraphic framework of the late Early Jurassic to early Late Jurassic strata from the Qaidam Basin (revised after Zhang, 1998; Lu et al., 2007, 2016, 2018, 2020c; Liu et al., 2013; Shao et al., 2014; Guo et al., 2020). Detrital Zircon U-Pb dating in Ma (million years) is from Yu et al. (2017) and Yang et al. (2017). Depositional environment based on Liu et al. (2013) and Lu et al. (2007, 2016, 2018, 2020c). Spore-pollen and flora fossils come from Liu et al. (2013). Abbreviations: Mts = Mountains; S = Stage; F = Formation; M = Member; De. = Depositional environment; D. = Delta; Flo. = Flora; CIA = *Coniopteris* initial appearance.

2011), south China (Huang, 2000; Deng et al., 2017), north China (Du et al., 1982; Du, 1985; Na et al., 2015; Deng et al., 2017), northwest China (Liu, 1993; Huang, 1995; Wang et al., 1998, 2005; Deng et al., 2017; Guo et al., 2020), and northeast China (Pu and Wu, 1982; Deng et al., 2017) have shown that vegetation and climate underwent significant changes in the Jurassic. A relatively arid late Early Jurassic climate gave way to a warm and humid climate in the early Middle Jurassic before arid conditions developed in the late Middle Jurassic. An intensification of the greenhouse effect is considered an important driver of this climatic change (Wang et al., 2005; Deng et al., 2017), but whether this was a function of volcanic activity is unclear.

Here, we investigate a terrestrial succession from the Dameigou section in the Qaidam Basin of the Qinghai-Tibet Plateau, China. We use a combination of palynology, organic carbon isotopes ($\delta^{13}C_{org}$), total organic content (TOC), kerogen macerals, and sedimentary Hg concentrations to evaluate the link between volcanism and contemporaneous changes in the terrestrial environment, climate, and flora during the Middle Jurassic.

2. Geological setting

The Qaidam Basin is located in the northeastern part of the Qinghai-Tibet Plateau, with an average elevation of about 3000 m and an area of about 120,000 km^2 (Lu et al., 2018, 2020b, 2020c). It is surrounded by the Kunlun Mountains to the south, the Altyn Mountains to the northwest, and the Qilian Mountains to the north (Lu et al., 2007, 2014a, 2014b, 2020c). During the Middle Jurassic, the Qaidam Basin was a site of major coal formation on the northern margin of the Tethys Ocean, with a paleolatitude of ~30° N (Wei, 2000; Lu et al., 2018, 2020c; Fig. 1a). The basement comprises Proterozoic metamorphic rocks, Ordovician flysch, Carboniferous clastic rocks and limestone, and volcanic rocks related to the Caledonian orogeny (Lu et al., 2007, 2014a, 2014b, 2016, 2018, 2020c). The main provenance area during the Middle Jurassic lay to the north in the Qilian Mountains, with a secondary provenance area in the Kunlun fold belt to the south (Yu et al., 2017; Fig. 1b, c).

The stratigraphic succession and inferred sedimentary environment, together with fossil plant and palynological assemblages from the late Early Jurassic to the early Late Jurassic of the Qaidam Basin are shown in Fig. 1d. The strata studied in this paper comprise the Dameigou Formation (= Dameigou 4th and 5th Member) and the Shimengou Formation (= Dameigou 6th and 7th Member) (Fig. 1d; Yang et al., 2006; Lu et al., 2007, 2014b, 2016, 2018, 2020b; Liu et al., 2013; Shao et al., 2014; Yu et al., 2017). The lower ~70 m of the Dameigou Formation is composed of gray-white conglomerate, conglomeratic sandstone, coarse sandstone, mudstone, and occasional thin coal seams, that were deposited in a fluvial sedimentary system. This part of the succession has been assigned an Aalenian age based on the presence of the *Coniopteris – Cladophlebis* fossil plant and the *Inaperturopollenites – Classopollis* fossil sporo-pollen assemblages (Zhang, 1998; Yang et al., 2006; Guo et al., 2020; Fig. 1d). The upper ~100 m of the Dameigou Formation comprises gray-black mudstone, carbonaceous mudstone and thick coal seams that were deposited in a swampy, deltaic sedimentary system. This part of the succession has been assigned a Bajocian age based on the presence of the *Coniopteris* Acme fossil plant and the *Cyathidites – Leiotriletes – Cycadopites – Disaccites* fossil sporo-pollen assemblages (Zhang, 1998; Yang et al., 2006; Guo et al., 2020; Fig. 1d). Zircon U-Pb dates from sandstones at the bottom (174 Ma) and middle (170 Ma) of the Dameigou Formation support these age assignments (Yang et al., 2017; Yu et al., 2017; Fig. 1d). The lower ~60 m of the Shimenigou Formation is composed of grayish-white fine to medium-grained sandstone and thin coal seams that were deposited in a deltaic sedimentary system. This strata has been assigned a Bathonian age based on the presence of the *Psophosphaera – Cycadopites* fossil sporo-pollen assemblage (Zhang, 1998; Yang et al., 2006; Guo et al., 2020; Fig. 1d). This is supported by a zircon U-Pb date of 168 Ma from the bottom of Shimengou Formation (Yang et al., 2017; Yu et al., 2017; Fig. 1d). The upper ~100 m of the Shimengou Formation is composed of black to gray-white thick shales that were deposited in a lacustrine sedimentary system. These strata are a prominent marker for regional correlation in the northern Qaidam Basin (Liu et al., 2013 and references therein). This part of the succession has been assigned a Callovian age based on the presence of the *Disaccites – Classopollis* fossil sporo-pollen assemblage (Liu et al., 2013 and references therein).

3. Materials and methods

We collected 64 fresh mudstone samples and 12 coal samples from the Dameigou and Shimengou formations and the upper part of the underlying Yinmagou Formation and the lower part of the overlying Caishiling Formation from the Dameigou section in the Qaidam Basin (sample levels are shown in Figs. 2 and 3). Each mudstone sample was first divided into two parts of which one was crushed into particles ca. 1 mm in diameter for analysis of (1) kerogen enrichment and (2) palynological isolation. The remaining part of the sample was crushed to pass through a 200 μm mesh and then divided into six subparts for analysis of (1) $\delta^{13}C_{org}$, (2) TOC, (3) total sulfur (TS), (4) major elements, (5) Hg concentration, and (6) pyrolysis.

$\delta^{13}C_{org}$, TS, and major elements were measured at the Beijing Research Institute of Uranium Geology, Hg concentrations were measured at the State Key Laboratory of Coal Resources and Safe Mining (Beijing), and TOC was measured at the Research Institute of Petroleum Exploration and Development Research (RIPED, Beijing). $\delta^{13}C_{org}$ analysis was performed using a stable isotope mass spectrometer (MAT253), and $\delta^{13}C_{org}$ values are expressed in per mil (‰) with respect to the Vienna Pee Dee Belemnite (VPDB) standard, with an absolute analysis error of ±0.1‰. TS analysis was performed using a carbon-sulfur analyzer (Eltra CS580-A) with a lower detection limit of 30 ppm, yielding an analytical accuracy within 5% of the reported values. Major elements analysis was undertaken with an X-ray fluorescence spectrometer (PW2404). The spectrometer was calibrated before use with standards of CRMs (GBW07427), and analytic precision was within 5%. Hg concentration was undertaken using a mercury analyzer (Lumex RA-915+) with lower detection limits of 2 ng/g (2 ppb). The Hg analyzer was calibrated before use with standards of China National Certified Reference Material soil (CRMs; GBW07427) with a Hg concentration of 52 ± 6 ppb, and analytic precision was within 5%. TOC analysis was performed using an elemental analyzer (Vario MICRO Cube). To quantify the analytical results of TOC, a certified reference material (L-alanine) was used during the analysis, yielding an analytical accuracy of 1.5% of the reported values. The analytic precision or error of all samples is based on reproducibility and repeats of the standard sample and standard samples were run after every five sample analyses.

Ten mudstone samples were selected for pyrolysis measurements at RIPED using an Oil and Gas Evaluation workstation (OEG-II) according to China National Standard (GB/T18602–2012). Kerogen enrichment and identification was performed on 45 of the 76 mudstone samples according to China national standard (SY/T5125–2014) at RIPED, with no less than 300 effective points per sample analyzed. Palynological isolation and identifications were undertaken for 20 of the 76 mudstone samples. Samples for palynology were subjected to acid digestion in 30% hydrochloric acid (HCl) and 38% hydrofluoric acid (HF). Heavy mineral separation was used to concentrate the sporomorphs and separate them from other components of the residue. For each spore-pollen sample, more than 100 sporomorphs were identified by the point-counting method under transmitted light microscopy (Olympus BX 41). All palynological slides are housed at the State Key Laboratory of Coal Resources and Safe Mining (Beijing). Percentages of spore and pollen taxa were calculated based on the sum of total sporomorphs. Palynological assemblages were identified by stratigraphically constrained cluster analysis (CONISS) using the Tilia software.

Sedimentary Hg concentration has been used to infer pulses of

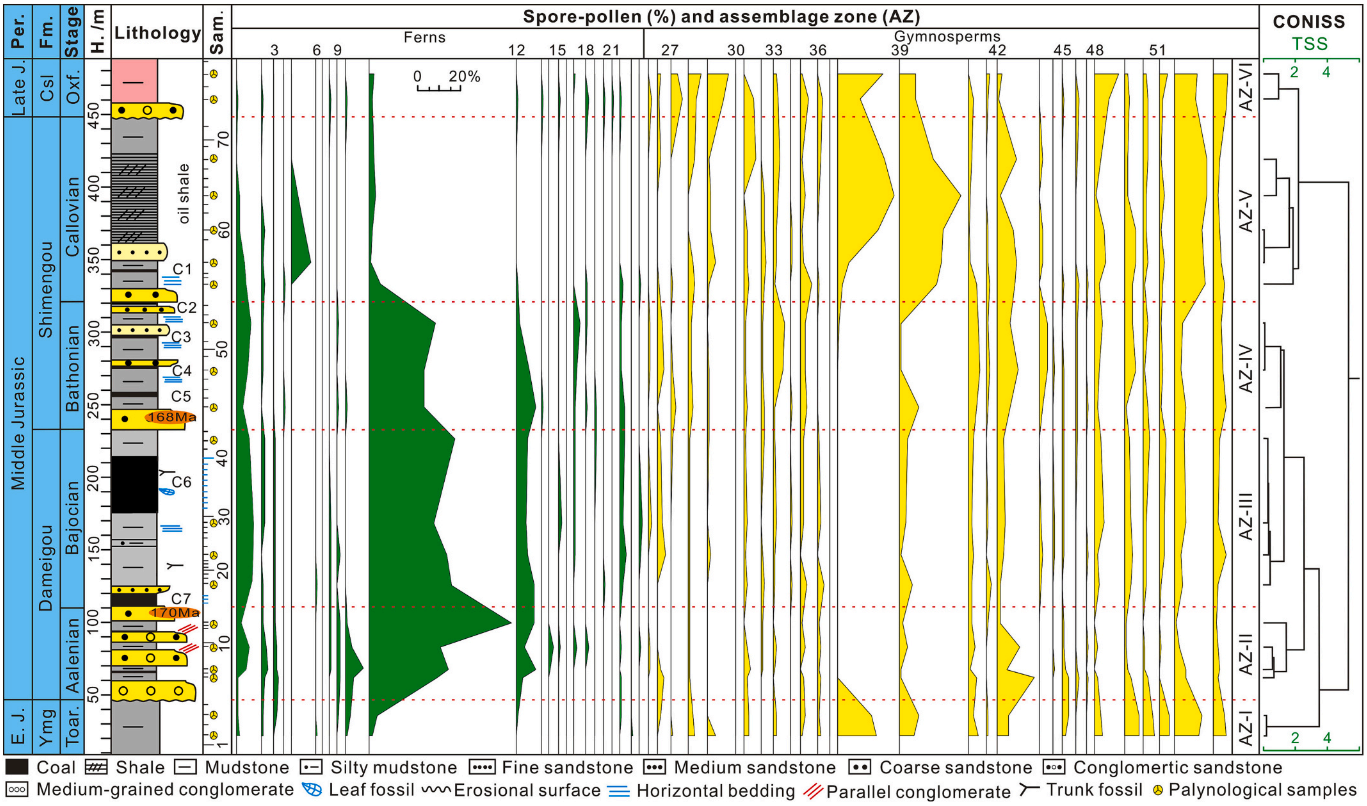

Fig. 2. Cumulative sporopollen summary diagram of the Dameigou section in the Qaidam Basin, with palynomorph percentages of the total spore-pollen sum plotted on the x-axis, and zones based on CONISS ordinations. C1 (Coal #1) to C7 (Coal #7) represent the position of individual coal marker beds. Note that palynological analyses were derived from 20 of the 76 mudstone samples. Abbreviations: E. J. = Early Jurassic; Per. = Period; J. = Jurassic; Ymg = Yinmagou; Csl = Caishiling; Fm. = Formation; Toar. = Toarcien; Oxf. = Oxfordian; H. = Height; Sam. = Sample; 1 = *Osmundacidites*; 2 = *Baculatisporites*; 3 = *Cibotiumspora*; 4 = *Lycopodiumsporites*; 5 = *Microfoveolatisporis*; 6 = *Laevigatosporites*; 7 = *Hymenophyllumsporites*; 8 = *Dictyophyllidites*; 9 = *Concavisporites*; 10 = *Matonisporites*; 11 = *Cyathidites*; 12 = *Deltoidospora*; 13 = *Granulatisporites*; 14 = *Apiculatisporis*; 15 = *Toroisporis*; 16 = *Densosporites*; 17 = *Asseretospora*; 18 = *Klukisporites*; 19 = *Biretisporites*; 20 = *Divisisporites*; 21 = *Undulatisporites*; 22 = *Calamospora*; 23 = *Verrucosisporites*; 24 = *Anapiculatisporites*; 25 = *Punctatisporites*; 26 = *Leiotriletes*; 27 = *Pinaceae*; 28 = *Pinuspollenites*; 29 = *Piceaepollenites*; 30 = *Cedripites*; 31 = *Podocarpidites*; 32 = *Parvisaccites*; 33 = *Callialasporites*; 34 = *Inaperturopollenites*; 35 = *Cycadopites*; 36 = *Chasmatosporites*; 37 = *Marsupipollenites*; 38 = *Classopollis*; 39 = *Concentrisporites*; 40 = *Cerebropollenites*; 41 = *Psophosphaera*; 42 = *Quadraeculina*; 43 = *Rotundipollis*; 44 = *Caytonipollenites*; 45 = *Eucommiidites*; 46 = *Alisporites*; 47 = *Pseudowalchia*; 48 = *Paleoconiferus*; 49 = *Protoconiferus*; 50 = *Protopinus*; 51 = *Pseudopicea*; 52 = *Piceites*; 53 = *Conifers* spp.; AZ-I to AZ-VI = the palynological assemblage zones (AZ) I to VI; CONISS = Stratigraphically constrained cluster analysis; TSS = Total sum of squares.

volcanic activity (e.g. Sanei et al., 2012; Grasby et al., 2019; Shen et al., 2019, 2020; Lu et al., 2020a, 2020b, 2021a, 2021b; Zhang et al., 2022). Variations in spore-pollen composition through the studied strata has been used to reconstruct paleoclimatic conditions based on the climatic preferences of the parent plants (Lu et al., 2021a; Wang et al., 2021; Zhang et al., 2022, 2023). Principal Components Analysis (PCA) by CANOCO software was performed to transform the relative abundances of spore-pollen into climatic parameters including temperature and humidity (Zhang et al., 2022). Spore and pollen data were ordinated using non-metric multidimensional scaling (nMDS) ordination analysis with the Bray–Curtis similarity matrix (at two dimensions; conducted using the PAST v3.11 software). This ordination method detects patterns of co-occurrence among taxa as well as ecological gradients (e.g., Mays et al., 2021). Kerogen macerals are used to identify sources of OM (Lu et al., 2021a; Xu et al., 2022; Zhang et al., 2022).

4. Results and analysis

4.1. *Paleofloral reconstruction and paleoclimatology based on palynological assemblages*

Twenty-seven spore, 26 pollen, and five algae genera have been identified in the studied material (Figs. 2, 3, 4; Table S1) and these are typical of late Early Jurassic and early Late Jurassic palynological assemblages (see Section 5.1). They are assigned to six palynological assemblage zones (AZ) based on the palynomorph abundance variations and CONISS: *Classopollis* – *Piceites* – *Concentrisporites* assemblage zone (AZ–I; #QD 1 – #QD 2), *Cyathidites* – *Quadraeculina* – *Deltoidospora* assemblage zone (AZ–II, #QD 3 – #QD 6), *Cyathidites* – *Osmundacidites* – *Deltoidospora* assemblage zone (AZ–III, #QD 7 – #QD 10), *Cyathidites* – *Quadraeculina* – *Deltoidospora* assemblage zone (AZ–IV, #QD 11 – #QD 13), *Concentrisporites* – *Classopollis* – *Piceites* assemblage zone (AZ–V, #QD 14 – #QD 18), and *Classopollis* – *Piceites* – *Paleoconiferus* assemblage zone (AZ–VI, #QD 19 – #QD 20) (Fig. 2). The composition of AZ-I is dominated by gymnosperm pollen (mean ($\bar{x}$) = 89.3%, including *Classopollis*, *Piceites*, and *Concentrisporites*), followed by fern spores ($\bar{x}$ = 10.7%, including *Cyathidites*, *Matonisporites*, and *Osmundacidites*), and a few algae ($\bar{x}$ = 4.50%) (Figs. 2, 3). The compositions of AZ-II and AZ-III are broadly similar: fern spores dominate ($\bar{x}$ = 68.7 and 62.5%) and include *Cyathidites*, *Deltoidospora*, and *Osmundacidites*, followed by gymnosperm pollen ($\bar{x}$ = 31.3 and 37.5%), including *Quadraeculina*, *Piceites*, and *Cerebropollenites*, while algae appear sporadically (Figs. 2, 3). The compositions of AZ-IV, AZ-V, and AZ-VI are noticeably different, although gymnosperm pollen ($\bar{x}$ = 51.7, 88.9, and 90.1%, respectively, including *Classopollis*, *Piceites*, and *Concentrisporites*) dominate followed by fern spores ($\bar{x}$ = 48.3, 11.1, and 9.90% respectively, including *Cyathidites* and *Osmundacidites*), but in AZ-IV fern spores had a higher content ($\bar{x}$ = 48.3%) and in AZ-V algae increased ($\bar{x}$ = 14.4%) (Figs. 2,

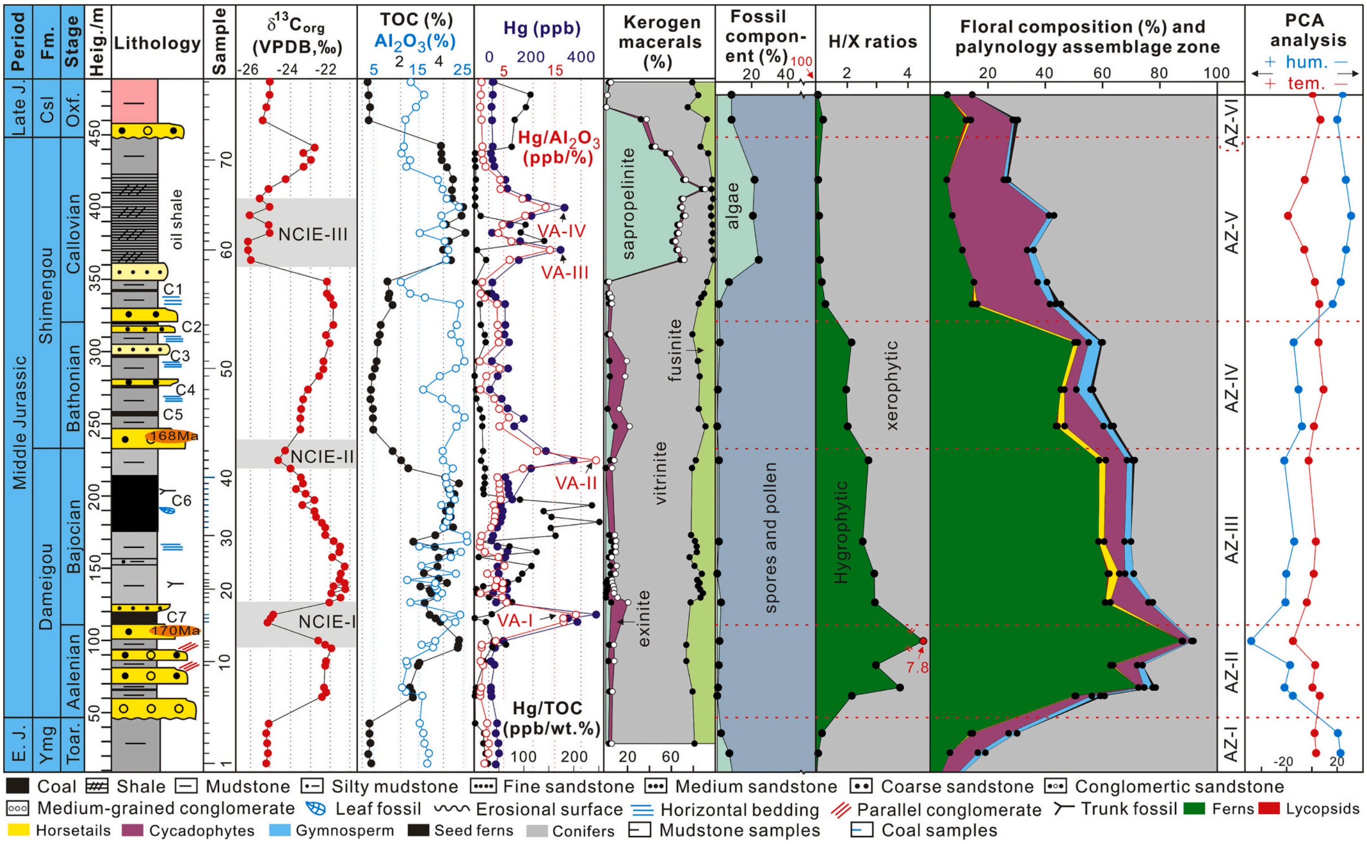

Fig. 3. Results of $\delta^{13}C_{org}$ analysis, TOC and Al_2O_3 contents, Hg concentrations, Hg/Al_2O_3 ratios, kerogen macerals, fossil component, hygrophytic/xerophytic (H/X) ratios, floral composition and palynology assemblage zone, and principal components analysis (PCA) from the Dameigou section in the Qaidam Basin. Abbreviations: E. J. = Early Jurassic; J. = Jurassic; Ymg = Yinmagou; Csl = Caishiling; Fm. = Formation; Toar. = Toarcien; Oxf. = Oxfordian; VPDB, Vienna Pee Dee Belemnite; CIE-I to CIE-III = three organic carbon isotope excursions; VA-I to VA-IV = four pulses of volcanic activity; AZ-I to AZ-VI = palynological assemblage zones (AZ) I to VI; PCA = principal component analysis; hum. = humidity; tem. = temperature.

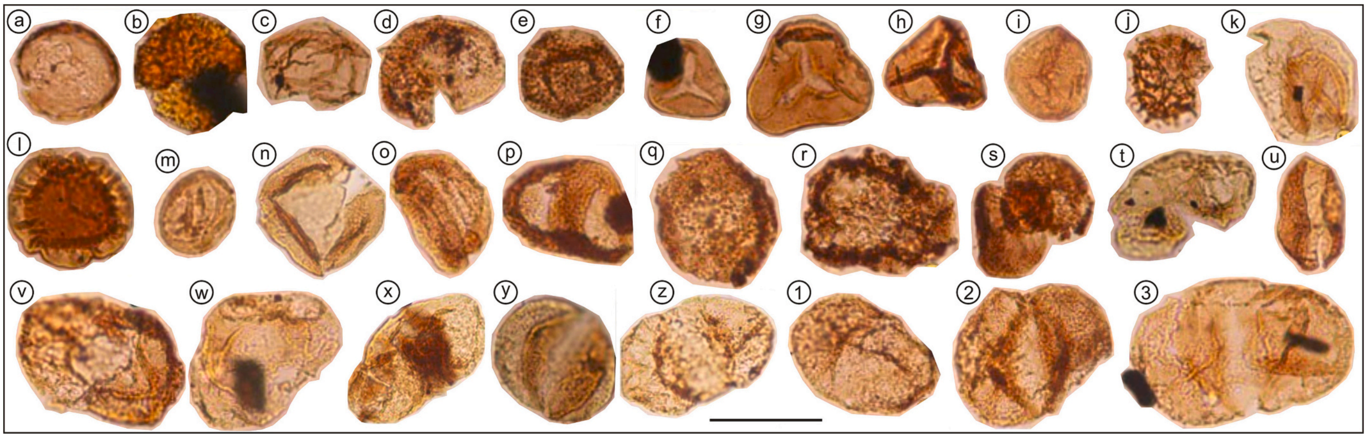

Fig. 4. Selected photos of representative palynological genera from Dameigou section in the Qaidam Basin (all scale bars = 50 μm). (a) = *Concentricystis* (#QD-6); (b) = *Botryococcus braunii* (#QD-19); (b) = *Calamospora* (#QD-14); (d) = *Anapiculatisporites* (#QD-9); (e) = *Osmundacidites* (#QD-15); (f) = *Cyathidites minor* (#QD-4); (g) = *Cyathidites australis* (#QD-5); (h) = *Matonisporites* (#QD-4); (i) = *Densosporites* (#QD-19); (j) = *Lycopodiumsporites* (#QD-14); (k) = *Concentrisporites* (#QD-17); (l) = *Callialasporites* (#QD-17); (m) = *Classopollis annulatus* (#QD-1); (n) = *Paleoconiferus* (#QD-19); (o) = *Quadraeculina ordinata* (#QD-18); (p) = *Quadraeculina limbata* (#QD-1); (q) = *Cerebropollenites carlylensis* (#QD-12); (r) = *Cerebropollenites findlaterensis* (#QD-3); (s) = *Podocarpidites* (#QD-18); (t) = *Pinuspollenites* (#QD-1); (u) = *Cycadopites* (#QD-19); (v) = *Pseudowalchia* (#QD-14); (w) = *Protopinus* (#QD-9); (x) = *Piceaepollenites* (#QD-15); (y) = *Pseudopicea* (#QD-4); (z) = *Protopinus* (#QD-4); (1) = *Chordasporites* (#QD-4); (2) = *Alisporites* (#QD-3); (3) = *Piceites* (#QD-19).

3).

The parent plants of the palynological taxa have been evaluated to reconstruct the floral successions of the Qaidam Basin (Fig. 3; Table S2). Diverse plant groups are recognized in the study area from the late Early Jurassic to early Late Jurassic including conifers ($\bar{x}$ = 47.0%), "filicalean" ferns ($\bar{x}$ = 37.3%), cycadophytes ($\bar{x}$ = 12.7%), horsetails ($\bar{x}$ = 1.00%), pteridosperms (seed ferns; $\bar{x}$ = 0.500%), and lycopsids ($\bar{x}$ = 0.100%) (Fig. 3; Table S1, S2). These taxa mainly grow in temperate to subtropical, warm and humid climates (Wang et al., 2005; Zhao et al., 2019; Lu et al., 2021a; Zhang et al., 2022). In AZ-I, AZ-V, and AZ-VI, conifers are dominant ($\bar{x}$ = 75.5, 61.6, and 77.5%, respectively, including Taxodiaceae, Cheirolepidiaceae, Pinaceae, and Podocarpaceae), followed by cycads ($\bar{x}$ = 13.5, 24.9, and 12.0%, respectively) and ferns ($\bar{x}$ = 10.3, 10.7, and 9.00%, respectively), while lycopsids, horsetails, and pteridosperms appear sporadically (Fig. 3; Table S1). In AZ-II to AZ-IV, ferns are dominant ($\bar{x}$ = 72.5, 60.0, and 46.5%, respectively, including Dipteridaceae/Matoniaceae, Dipteridaceae, Osmundaceae, Pteridaceae, Marattiaceae, Lygodiaceae, Dicksoniaceae, and Dicksoniaceae/Cyatheaceae), followed by conifers ($\bar{x}$ = 21.5, 27.6, and 39.8%, respectively) and cycads ($\bar{x}$ = 4.50, 7.90, and 7.50%, respectively) (Fig. 3; Table S1). Horsetails are less abundant, while lycopsids and pteridosperms appear sporadically (Fig. 3; Table S1).

Results of PCA analysis based on the relative abundance of spore-pollen genera are shown in Figs. 3, 5, and 6. Two main ordination axes representing the largest variance in palynological composition are used to explain the two most dominant environmental gradients that control the dataset (e.g., Li et al., 2020; Zhang et al., 2022). In this study, axis 1 and axis 2 separately account for 78.4 and 7.21% of the sporomorph spectra difference (Fig. 5a). On the positive side of axis 1, the xerophytic *Classopollis* and *Piceites* pollen have high scores (e.g., Jin et al., 2022; Zhang et al., 2022), and the hygro-mesophytic *Cyathidites* spores and other hygrophytic spores show high scores on the negative side of axis 1 (e.g., Li et al., 2020; Zhang et al., 2022; Figs. 5a, 6). Relatively cool, temperate conifer pollen including *Quadraeculia*, *Paleoconiferus*, and undifferentiated conifers have high scores on the positive side of axis 2, and the relatively warm-preference fern spores *Cyathidites* and conifer pollen *Classopollis* have high scores on the negative side of axis 2 (e.g., Li et al., 2020; Zhang et al., 2022). Thus, the first and the second axes are interpreted to reflect the changes in relative humidity and temperature, respectively (Figs. 3, 5). The PCA results indicate relatively warm and dry climatic conditions prevailed during AZ-I, AZ-V, and AZ-VI, and relatively cool and humid climatic conditions prevailed during AZ-II, AZ-III, and AZ-IV (Fig. 3). There were three episodes of temperature increase (during which the proportions of warm-loving plants increased) with approximate temporal coincidence with the NCIEs and excess loading of Hg to the sediment (seen in the Hg/Al_2O_3 data; see Fig. 3, Section 4.2 and 4.4).

According to the climatic affinity of the palynological fossils, identified spores and pollens were classified into hygrophytes and xerophytes. The hygrophytic/xerophytic (H/X) ratio is a first-order approximation of a humidity signal, unless any of the exceptions mentioned occur in high abundance (Mueller et al., 2016a, 2016b). We follow previous studies in which all spores are classified as hygrophytes together with the *Alisporites*, *Aulisporites*, and *Cycadopites* groups, and all remaining pollen are classified as xerophytic (Mueller et al., 2016a, 2016b). The H/X ratios are shown in Table S1. H/X varies from 0.070 to 7.82 ($\bar{x}$ = 1.21) and increased in AZ-II and AZ-III (Fig. 3).

Results of nMDS analysis based on the relative abundance of spore-pollen genera are shown in Fig. 5b. In this study, as shown in the discrete areas in ordination space of the nMDS plot (Fig. 5b), the distribution of palynological fossils is consistent with relatively warm and arid climatic conditions in AZ-I, AZ-V, and AZ-VI, and relatively cool and humid climatic conditions in AZ-II to AZ-IV (inferred from the palynological abundance change and PCA analysis). Furthermore, palynological fossils record two obvious floral changes on the nMDS plot. The first occurred at the Toarcian-Aalenian boundary (= the Early Jurassic-Middle Jurassic boundary; AZ-I to AZ-II), and the second occurred at the Bathonian-Callovian boundary (Middle Jurassic; AZ-IV to AZ-V). These samples plot a distance from those of the Early Jurassic Aalenian and Bajocian stages (Fig. 5b), indicating a significantly different plant taxonomic composition at those times.

4.2. Total organic carbon (TOC) and $\delta^{13}C_{org}$ chemostratigraphy

Results for TOC and $\delta^{13}C_{org}$ are shown in Fig. 2 and Table S3. TOC values vary from 0.310 to 5.00 wt% ($\bar{x}$ = 2.84 wt%), with three relatively low-value intervals and two relatively high-value intervals (Fig. 3). Relatively low TOC values were found in samples 1 to 5 ($\bar{x}$ = 0.370 wt%), samples 44 to 58 ($\bar{x}$ = 0.870 wt%), and samples 73 to 76 ($\bar{x}$ = 0.360 wt%). Relatively high TOC values were found in samples 6 to 43 ($\bar{x}$ = 3.61 wt%) and 59 to 72 ($\bar{x}$ = 4.40 wt%). From samples through the complete succession, the peak temperature of rock pyrolysis (T*max*) values vary from 429 to 442 °C ($\bar{x}$ = 438 °C) (Table S4) and indicate that kerogen maturity varies from low-maturity to mature as defined by the China National Standard (SY/T 5477–2003) (Table S5).

$\delta^{13}C_{org}$ values vary from −26.1‰ to −21.0‰ ($\bar{x}$ = −23.3‰), showing five lighter plateaus and four heavier plateaus (Fig. 3). Relatively low $\delta^{13}C_{org}$ values were found in samples 1 to 5 ($\bar{x}$ = −25.2‰), samples 14 to 16 ($\bar{x}$ = −25.0‰, NCIE-I), samples 41 to 43 ($\bar{x}$ = −24.5‰, NCIE-II), samples 59 to 68 ($\bar{x}$ = −25.5‰, NCIE-III), and samples 73 to 76 ($\bar{x}$ = −25.7‰). Relatively high $\delta^{13}C_{org}$ values were found in samples 6 to 13 ($\bar{x}$ = −22.3‰), samples 17 to 40 ($\bar{x}$ = −22.2‰), samples 44 to 58 ($\bar{x}$ = −22.3‰), and samples 69 to 72 ($\bar{x}$ = −23.3‰) (Fig. 3).

4.3. Kerogen macerals and a potential source of organic matter

Results for kerogen macerals are shown in Fig. 3 and Table S4.

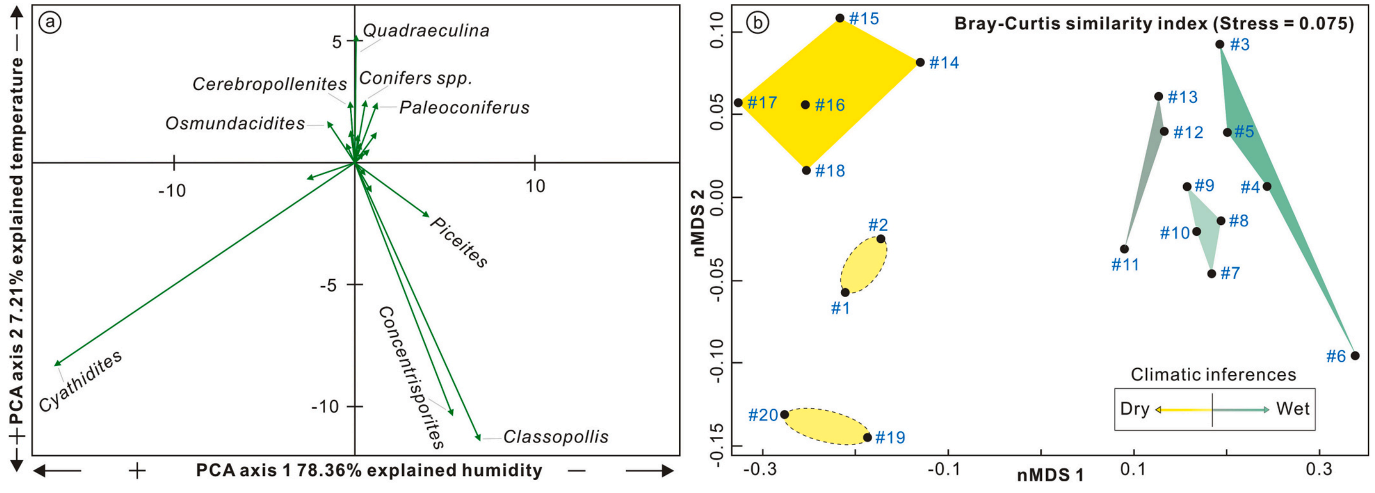

Fig. 5. Principal Component Analysis (PCA) ordination plot of sporomorph relative abundances from the Dameigou section in the Qaidam Basin.

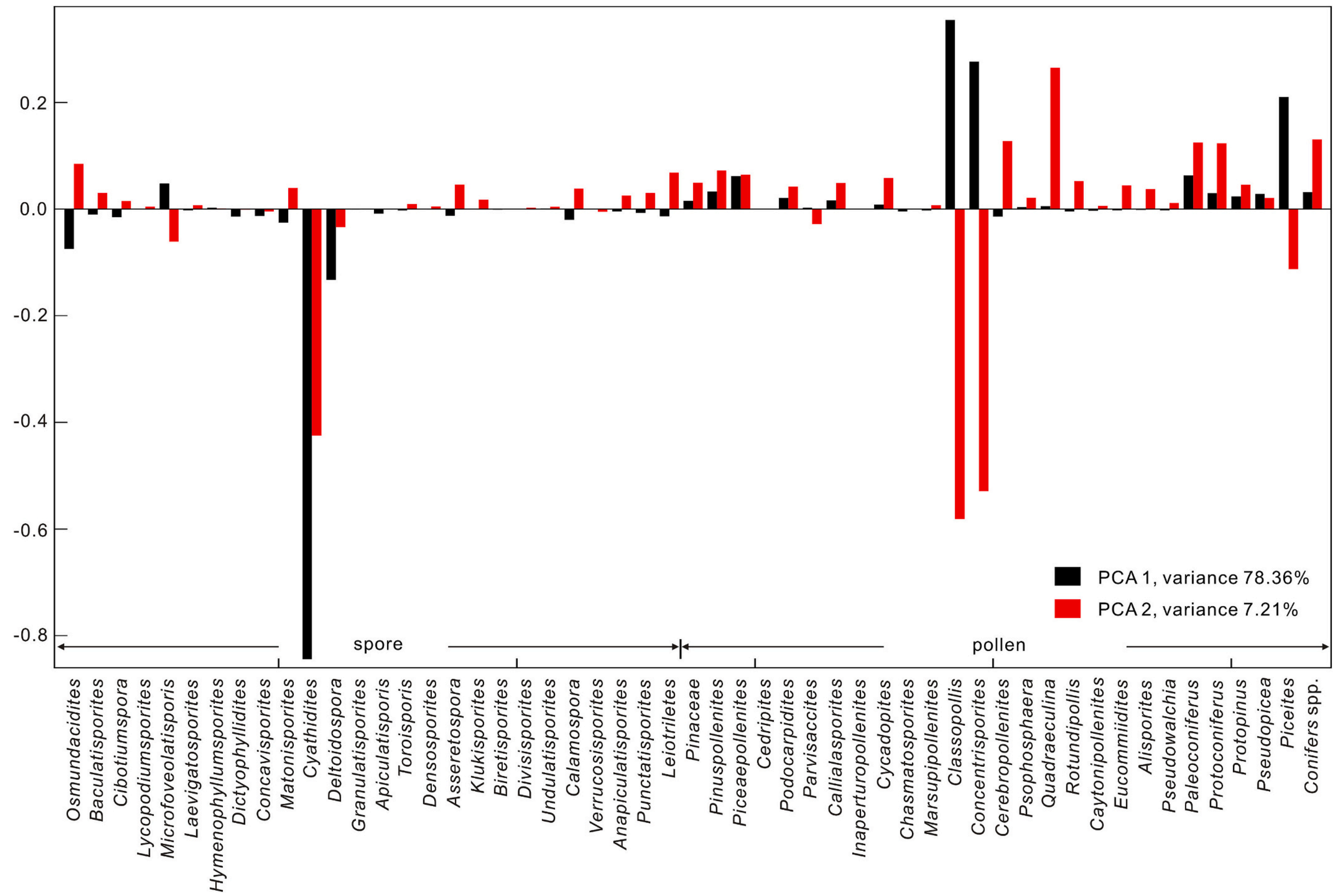

Fig. 6. Loading plots of PCA1 and PCA2 for spore and pollen genera from the Dameigou section in the Qaidam Basin.

Kerogen macerals mainly comprise vitrinite ($\bar{x} = 61.5\%$), sapropelinite ($\bar{x} = 20.3\%$), and fusinite ($\bar{x} = 13.5\%$), followed by exinite ($\bar{x} = 4.70\%$) (Figs. 3, 7; Table S4). Vitrinite content varies from 5.6 to 89.4% ($\bar{x} = 61.5\%$) and comprises non-fluorescent telinite and collinite (Figs. 3, 7a). Sapropelinite content varies from 0.0 to 87.8% ($\bar{x} = 20.3\%$) (Figs. 3, 7f-i). Fusinite content varies from 1.6 to 26.4% ($\bar{x} =$

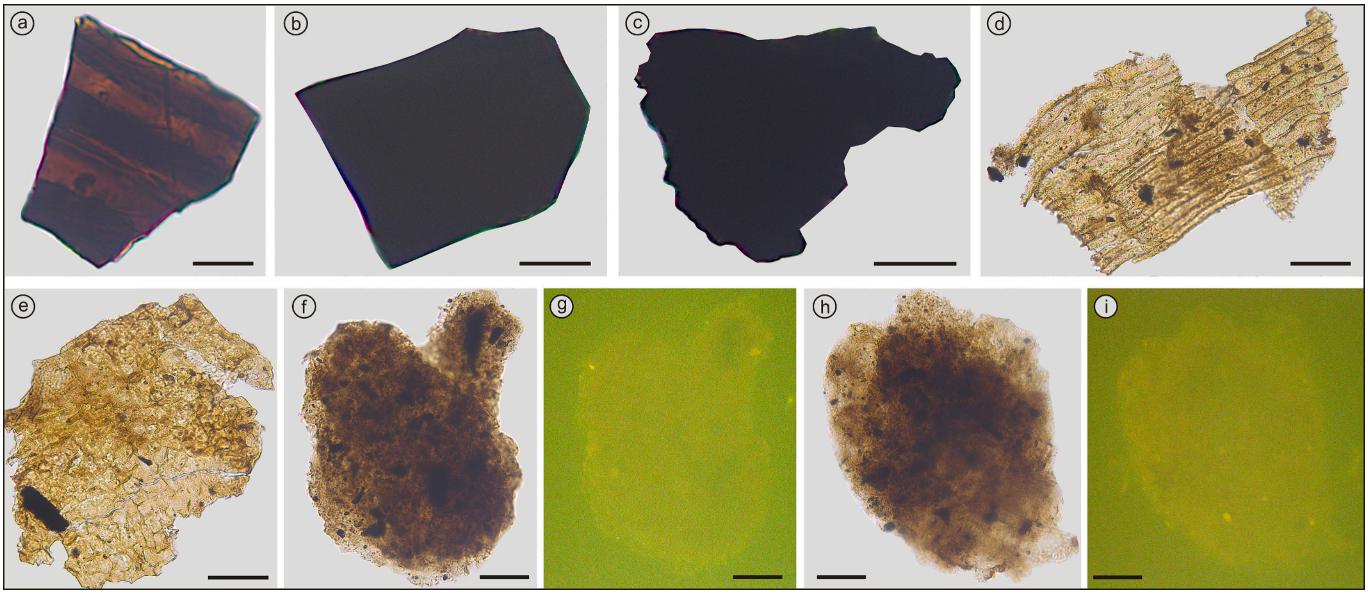

Fig. 7. Photomicrographs showing microstructure characteristics of kerogen macerals in the Qaidam Basin (all scale bars = 50 μm). (a) vitrinite (transmitted light, sample #20); (b,c) inertinite (transmitted light, samples #18 and #48); (d) suberinite (transmitted light, sample #70); (e) cutinite (transmitted light, sample #17); (f and g) saporopollenite (transmitted light and fluorescence, respectively, sample #67); (h and i) saporopollenite (transmitted light and fluorescence, respectively, sample #58).

13.5%) (Figs. 3, 7b, 7c). Exinite content varies from 0.0 to 15.9% ($\bar{x}$ = 4.70%) and mainly comprises sporopollenite, cutinite, and subertinite (Figs. 3, 7d, 7e). Previous studies showed that the vitrinite, inertinite, and exinite maceral groups are derived principally from terrestrial higher plants, whereas the sapropelinite group is derived from lacustrine plankton, predominantly algae (e.g., Lu et al., 2021a; Xu et al., 2022; Zhang et al., 2022). In this study, vitrinite, inertinite and chitinite were dominant in samples 3 to 58 and 74 to 76 (Fig. 3), indicating that terrestrial higher plants were the main source of OM. Samples 59 to 73 showed a significant increase in sapropelinite content (Fig. 3), indicating a shift from a terrestrial OM source to a mixed source of terrestrial plants and lacustrine algae. This shift occurred at a time during which the sedimentary environment changed from deltaic to semi-deep/deep lake (Fig. 1d) and sees an increase in algal content (Fig. 3) and a decrease in C/N ratios (Li et al., 2020).

4.4. *Mercury anomalies as a proxy for volcanism*

Sedimentary Hg concentrations are shown in Fig. 3 and Table S3. These data reveal considerable variation, ranging from 5.14 to 475 ppb ($\bar{x}$ = 76.2 ppb) and have a distribution that is broadly anticorrelated to $\delta^{13}C_{org}$ values (Fig. 3). Application of the Hg volcanism proxy requires an understanding of its sedimentary host phases. Most studies have assumed organic matter to be the dominant host of Hg, normalizing mercury to total organic carbon (Hg/TOC) in order to identify Hg enrichments that are not a function of elevated organic carbon content in ancient sediments (Ravichandran, 2004; Shen et al., 2019 and references therein). However, Hg can be also associated with the sulfide (Bower et al., 2008) or clay fractions of the sediment (Farrah and Pickering, 1978). The exact controls on Hg-host phase associations are not well understood, but uptake of Hg by sulfides appears to be associated with intensely reducing conditions, which leads to high stability constants for inorganic Hg-S complexes (Bower et al., 2008). Clay minerals are also capable of adsorbing Hg, leading to significant Hg enrichments in sediments (Farrah and Pickering, 1978). In this study, the Hg concentrations show stronger covariation with Al_2O_3 (r = +0.470, number of samples [n] = 76) than with TOC (r = +0.190) or TS (r = +0.070) (Fig. 8), suggesting clay minerals may be an important host of Hg. As a result, we employ Hg/Al_2O_3 values as a proxy for volcanism (Fig. 3, see also Hg/TOC values plotted on this figure). Hg/Al_2O_3 varies from 0.320 to 23.2 ppb/% ($\bar{x}$ = 4.08 ppb/%) with distribution broadly similar to the raw Hg concentrations (Fig. 3). There are four Hg/Al_2O_3 peaks with values of 19.2 ppb/% (from which we infer pulses of volcanic activity = VA-I), 23.2 ppb/% (VA-II), 14.1 ppb/% (VA-III) and 13.3 ppb/% (VA-IV; Fig. 3) and these approximately correspond to the level of the NCIEs (Fig. 3).

5. Discussion

5.1. *Stratigraphic correlation*

There are still some discrepancies in the age attribution of the Caishiling Formation in published stratigraphic schemes for the Qaidam Basin. Some have assigned the formation to the Middle Jurassic Callovian stage (Zhang, 1998; Wang et al., 2005), while others have assigned it to the Late Jurassic Oxfordian stage (Lu et al., 2007, 2014b, 2018; Yan et al., 2007; Liu et al., 2013; Shao et al., 2014; Deng et al., 2017). In this study, the latter stratigraphic scheme is adopted (see Section 2) because this assignment is consistent with our bio- and chemostratigraphic framework (see below).

The composition of palynological fossil assemblages is an effective biostratigraphic tool (e.g., Wang et al., 2005; Yang et al., 2006; Guo et al., 2020; Lu et al., 2021a; Zhang et al., 2022, 2023). In this study, there are no rib-bisaccate palynological fossils (e.g., *Taeninaesporites*, *Protohaploxypinus*, and *Chordasporites*), all forms that had been widespread in the Triassic, rare in the Early Jurassic, and had disappeared by the Middle Jurassic (Liu, 1990; Huang and Li, 2007; Zhao et al., 2019). Similar assemblages to those seen in this study are known from the Yanan Formation in the Shaanxi-Gansu-Ningxia Basin (Xu and Zhang, 1980), the Datong Formation in Shanxi Province (Liu, 1986b), and the Shaogou Formation in the Baotou area (Liu, 1982) from North China, the Xiangxi Formation in Hubei Province (Li and Shang, 1980) and the Fengxian Formation (Wang and Tong, 1982) and the Xiangshan Formation (Huang, 2000) in Jiangsu Province from South China, the Xishanyao Formation in the Shanwan area and Wenquan coalfield from northwest China (Liu, 1990; Liu and Sun, 1992), the United Kingdom (Couper, 1958), Canada (Pocock, 1970), Russia (Vakhrameev, 1991; Rostovtseva, 2011), and Antarctica (Shang, 1997). Meanwhile, palynological fossils of *Trilobosporites*, *Cicatricosporites*, and *Schizaeoisporites*, which flourished in the Early Cretaceous and are known in small numbers or individually in the Late Jurassic of China, are absent from our studied strata. Similar records are seen in the Anding Formation in the Shaanxi-Gansu-Ningxia Basin (Xu and Zhang, 1980) and the Houcheng Formation in Hebei Province (Zhang, 1989) from North China and the Penglaizhen Formation from South China (Zhang, 1987).

Comparative analysis of characteristic palynomorphs from the study area and other sections around the world provides further constraint on their stratigraphic assignment. The palynological fossils from AZ-II to AZ-III in the study area can be compared with the Middle Jurassic palynological assemblages of the Xishanyao (Sun, 1989) and Miyaogou (Huang, 1995) formations in the Turpan-Hami Basin and the Xishanyao Formation in southern Jungeer Basin (Zhang, 1990) and the Qitaibeishan coalfield (Liu, 1993) from northwest China, the Yan'an Formation in the Shaanxi-Gansu-Ningxia Basin (Du et al., 1982), the Yan'an (Du et al., 1982) and Longfengshan (Du, 1985) formations in Gansu

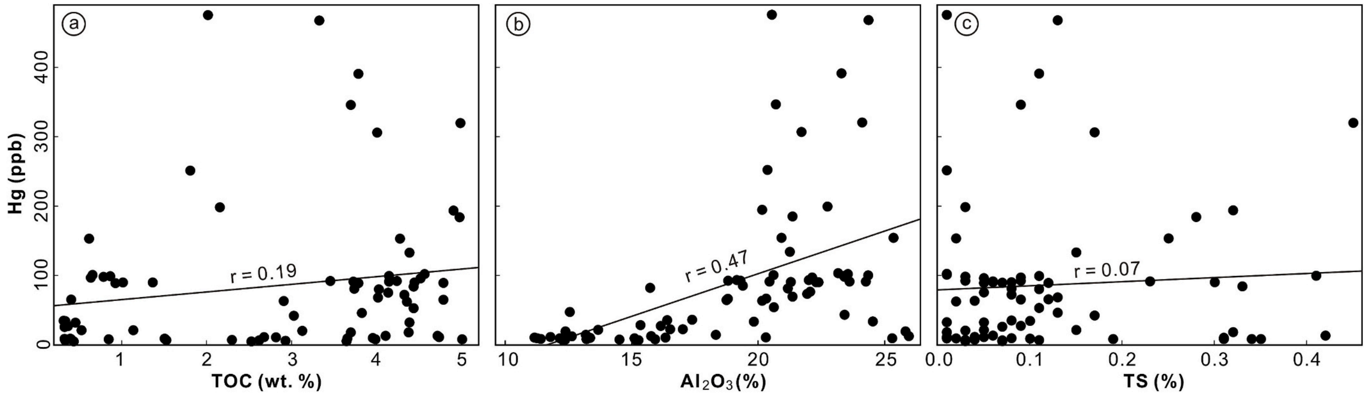

Fig. 8. Plots showing Hg concentrations versus (a) TOC, (b) Al_2O_3, and (c) TS from all samples (n = 76) in the Dameigou section. Plots show that Hg concentrations show stronger covariation with Al_2O_3 (r = +0.47) than with TOC(r = +0.19) or TS (+0.07).

Province, the Datong Formation in North China (Liu, 1986b), and the Beipiao Formation in the west of Liaoning Province in northeast China (Pu and Wu, 1982). These records are dominated by *Cyathidites* (*Cyathidites minor*), *Deltoidospora*, *Osmundacidites*, and *Quadraeculina*, and contained more *Cycadopites*, *Eucommiidites*, *Podocarpidites*, *Piceites*, and *Pinuspollenites*. A key difference is the lower abundance of *Callialasporites* and *Lycopodiumsporites* in AZ-II and AZ-III in this study. Similar records were observed in the early Middle Jurassic palynological assemblages in Siberia (Russia) (c.f. Wang et al., 1998) and Yorkshire (United Kingdom) (Couper, 1958) where they are characterized by the high content of *Cyathidites minor*. This element first appeared in the Late Triassic, began to develop in the Early Jurassic, and reached its peak in the Middle Jurassic and its high content is also considered characteristic for palynological assemblages of Middle Jurassic age (Wang et al., 1998; Zhao et al., 2019).

Between AZ-IV and AZ-V, the abundance of *Cyathidites minor* and other fern spores decreases, gymnosperm pollen begins to dominate, and the abundance of *Classopollis* pollen begins to increase before peaking in AZ-V (Fig. 2). These two palynological assemblage zones approximately correlate (stratigraphically) to the Toutunhe Formation in the Junggar Basin (Zhang, 1990) and the Meiyaogou Formation in the Turpan-Hami Basin (Huang, 1995) in northwest China, the Zhiluo and Anding formations in Shaanxi Province (Xu and Zhang, 1980) and the Wangjiashan Formation in Gansu Province (Du, 1985) in North China, and the Lanqi and Guojiadian formations in the west of Liaoning Province in northeast China (Pu and Wu, 1982). These areas record similar palynological assemblages (dominated by gymnosperm pollen followed by fern spores) and see a similar increase in the abundance of *Classopollis* pollen. In Eurasia, the abundance of *Classopollis* pollen decreased significantly in the early Middle Jurassic, then increased and peaked in the late Middle Jurassic (Vakhrameyev, 1982; Rostovtseva, 2011). In summary, we consider that the palynological fossils of the Dameigou and Shimengou formations in the study area to be consistent with a Middle Jurassic age assignment.

Chemostratigraphy, and in particular the carbon isotope record, can further constrain the stratigraphy in our study area. Numerous major events in Earth's history (e.g., Late Paleozoic glacial events, the Permian-Triassic mass extinction, the Carnian Pluvial Event, the Triassic-Jurassic mass extinction, and the Toarcian Oceanic Anoxic Event) are accompanied by global carbon cycle fluctuations preserved in the record of organic and inorganic carbon isotopes, and these provide a basis for comparing strata deposited in a diverse range of depositional environments (e.g., Dal Corso et al., 2018; Jin et al., 2020, 2022; Lu et al., 2020a, 2020b, 2021a, 2021b; Zhang et al., 2022). However, terrestrial $\delta^{13}C_{org}$ is a complicated system that is readily affected by diagenesis, OM sources and plant types (e.g., Schouten et al., 2007; Oehlert and Swart, 2014). The influence of these factors must be accounted for when using $\delta^{13}C_{org}$ records for stratigraphic correlation.

In our study, pyrolysis data indicates that diagenetic processes are unlikely to be responsible for the observed shifts in the $\delta^{13}C$ signature of the OM because such changes occur in late diagenetic to metamorphic burial stages that our material has not been subjected to (Dal Corso et al., 2018). The $\delta^{13}C_{org}$ disturbances in the studied strata are also unlikely to have occurred through proportionate changes in terrestrial and algal organic carbon sources, which can be isotopically distinct from one another (Cloern et al., 2002). Variations in kerogen macerals reveal a change in OM sources from terrestrial plants sources in the Dameigou Formation to the mixed terrestrial plants and lacustrine plankton sources (from samples 59 to 73) in the Shimengou Formation (Fig. 3). Similar trends in OM sources were further supported by changes in the C/N ratios in the study area (Li et al., 2020). Importantly, no apparent relationship exists between OM sources (including kerogen macerals and C/N ratios) and $\delta^{13}C$ values during the Middle Jurassic. Furthermore, the $\delta^{13}C_{org}$ is largely limited by the pathway of plant photosynthesis and varies with plant types (e.g., Guo et al., 2020; Zhang et al., 2022). Although the occurrence of plant type changes in the upper part of the Shimengou Formation may have been a factor in NCIE-III (Figs. 2, 3), this seems unlikely to be responsible for the variation in the $\delta^{13}C_{org}$ of the studied strata, because similar trends in carbon isotopes have been documented in carbonates and bulk marine and terrestrial OM (Fig. 9).

A compilation of Middle Jurassic global $\delta^{13}C$ data reveals distinctive patterns in both marine and continental records, in which four PCIEs during the Aalenian, the early Bajocian, at the Bathonian-Callovian boundary, and at the Callovian-Oxfordian boundary interspersed with three NCIEs at the Aalenian-Bajocian boundary, at the Bajocian-Bathonian boundary, and in the middle Oxfordian (e.g., Bartolini et al., 1999; Bartolini and Cecca, 1999; Jenkyns et al., 2002; Hesselbo et al., 2003; O'Dogherty et al., 2006; Schlaich and Aigner, 2017; Fig. 9). Our study also recognizes these $\delta^{13}C_{org}$ patterns (Figs. 3, 9, see also Section 5.2) facilitating comparison with other Middle Jurassic sections around the world (Fig. 9). Therefore, we consider that the $\delta^{13}C_{org}$ record in the studied strata represent global carbon cycle fluctuations during the Middle Jurassic. .

In summary, we consider that the stratigraphic scheme adopted in this study is reliable, and that the Dameigou Formation is of Middle Jurassic Aalenian-Bajocian age and the Shimengou Formation is of Middle Jurassic Bajocian-Callovian age. The overlying Caishiling Formation dates to the Late Jurassic Oxfordian Stage.

5.2. Middle Jurassic terrestrial environmental and floral changes

The Middle Jurassic was a time of significant changes in global environments and climates, characterized by global carbon isotope fluctuations and changes in terrestrial plant assemblages (Jenkyns et al., 2002; Hesselbo et al., 2003; Dera et al., 2011; Rostovtseva, 2011; Deng et al., 2017; Al-Mojel et al., 2018). The Middle Jurassic plant communities and paleoclimates detailed in this study also underwent significant changes. Arid-loving conifer communities of the late Early Jurassic Toarcian stage were replaced by humid-loving ferns during the Middle Jurassic Aalenian-Bajocian stages, before conifers returned during the Middle Jurassic Bathonian to the early Late Jurassic Oxfordian (Figs. 2, 3). Results of PCA, H/X ratios, and nMDS analysis provide further evidence of floral and paleoclimatic changes in the study area (Figs. 2, 3, 5; see Section 4.1). Similar floral and climatic changes have been observed in other regions such as northwest China (Sun, 1989; Zhang, 1990; Huang, 1995; Wang et al., 1998, 2005; Deng et al., 2017; Zhao et al., 2019), North China (Xu and Zhang, 1980; Du et al., 1982; Du, 1985; Liu, 1986a; Na et al., 2015; Deng et al., 2017), northeast China (Pu and Wu, 1982; Deng et al., 2017), South China (Meng, 1999; Huang, 2000; Deng et al., 2017), United Kingdom (Couper, 1958), and Russia (Rostovtseva, 2011).

Results of the PCA analysis show that three warming events in the studied area occurred in the Middle Jurassic and correspond to the NCIEs (Figs. 3, 5, 6). The warming trend is supported by changes in global oxygen isotope data (Dera et al., 2011; Fig. 9). In this study, the warming events associated with NCIE-I and NCIE-II were accompanied by relatively humid conditions (Figs. 3, 9). This is inferred from the combined results of the dominant fern spores, PCA, H/X ratio, and nMDS analysis (Figs. 2, 3, 5, 6). In contrast, the warming associated with NCIE-III was accompanied by relatively arid conditions (Figs. 3, 9). This is inferred from the combined results of the rapidly increasing *Classopollis* content, PCA, H/X ratio, and nMDS analysis (Figs. 2, 3, 5, 6). Drought-like conditions expanded significantly not only across South and North China (Deng et al., 2017 and references therein) but also across Central Asia, Siberia, and Europe (Vakhrameev, 1991; Dera et al., 2011; Rostovtseva, 2011), as had been the case in the Early Jurassic Toarcian Stage (Deng et al., 2017; Jin et al., 2020, 2022; Lu et al., 2020b).

5.3. Volcanism as a driver of Middle Jurassic change

In recent years, volcanic activity has been identified as one of the main drivers of global environmental, climatic, and floral changes (e.g.,

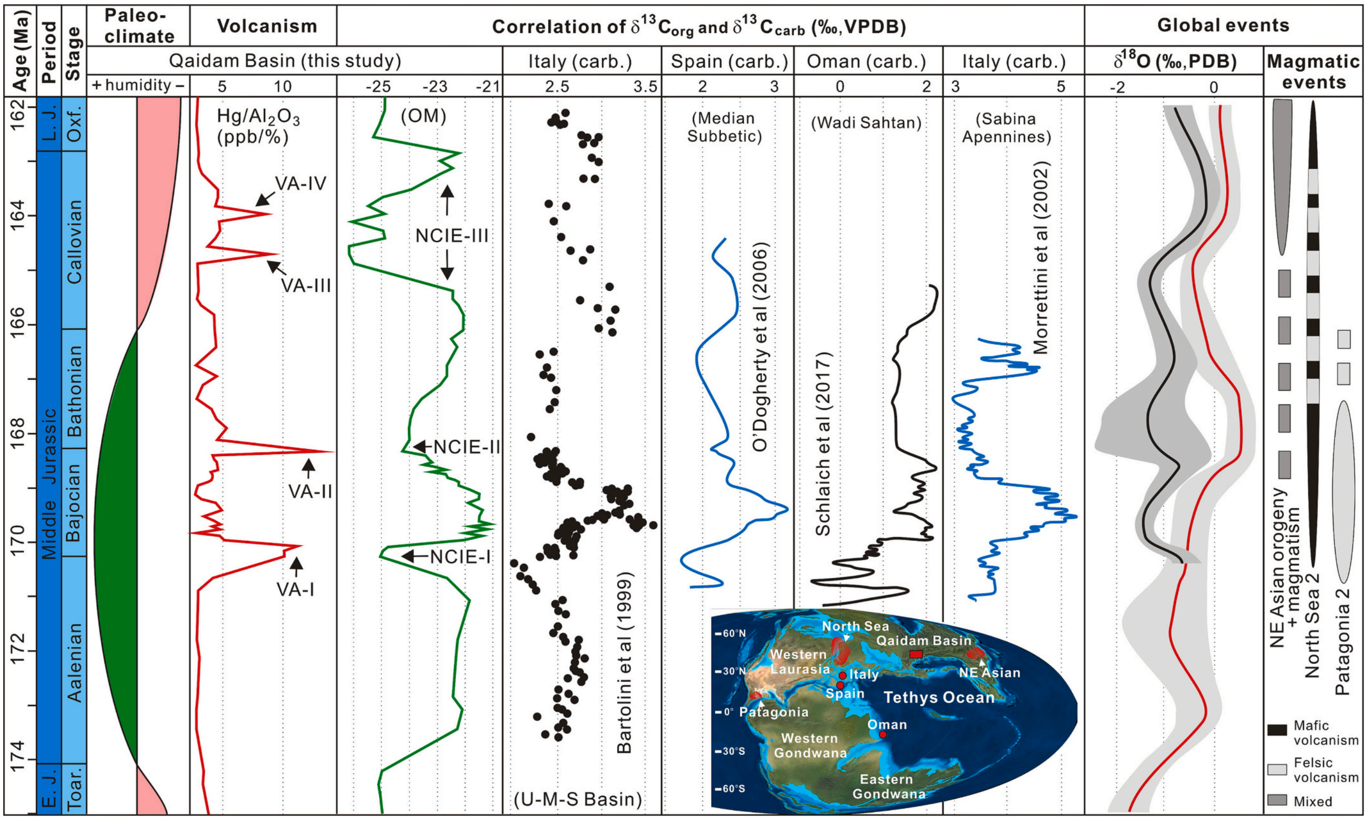

Fig. 9. Correlations of paleoclimate, volcanism, $\delta^{13}C_{org}$ and $\delta^{13}C_{carb}$ isotope records, and global events from late Toarcian to early Oxfordian Stages of the Jurassic Period. $\delta^{18}O$ curves modified from Dera et al. (2011) and references therein. Magmatic events modified from Pankhurst et al. (2000), Wu et al. (2000, 2001), Dera et al. (2011) and references therein, and Huang (2019). Paleogeographic reconstruction for the Middle Jurassic world modified from the ~170 Ma map of the webpage https://deeptimemaps.com/global-paleogeography-and-tectonics-in-deep-time. Abbreviations: J. = Jurassic; Toar. = Toarcian; Oxf. = Oxfordian; OM = organic matter; carb. = carbonate; VPDB, Vienna Pee Dee Belemnite; CIE-I to CIE-III = three organic carbon isotope excursions; VA-I to VA-IV = four pulses of volcanic activity.

Pyle and Mather, 2003; Grasby and Beauchamp, 2009; Grasby et al., 2011, 2015, 2016, 2020; Sanei et al., 2012; Shen et al., 2019, 2020, 2022a; Them et al., 2019; Lu et al., 2020a, 2020b, 2021a; Zhang et al., 2022, 2023; Zhou et al., 2022). We identified four Hg (and Hg/Al_2O_3) anomalies that are significantly higher than background levels seen in surrounding strata (Fig. 3). In terrestrial lake settings, Hg can be sourced from the atmosphere (i.e., that linked to major volcanism) as well as from hydrological runoff (Shen et al., 2019, 2020; Lu et al., 2021a; Zhang et al., 2022). Clay minerals are the main host of Hg in our study materials but samples with elevated Al_2O_3 concentrations in the strata pre- and post-NCIEs are not also enriched in Hg (Fig. 3), suggesting that where terrestrial clay minerals are enriched in Hg this was due to input from contemporaneous large-scale volcanism.

The temporal coincidence of $\delta^{13}C_{org}$ shifts and Hg (and Hg/Al_2O_3) anomalies in the study area also suggests that Hg was sourced from volcanism (Fig. 3). The record of $\delta^{13}C_{org}$ is considered to be an effective indicator of atmospheric CO_2 change in Earth's history (e.g., Wu et al., 2021; Xu et al., 2022). Volcanic eruptions and intrusions can release large amounts of CO_2 and Hg, leading to an increase in Hg concentration and atmospheric pCO_2 and fall in the contemporaneous atmospheric $\delta^{13}C$ value (Shen et al., 2019, 2022a; Vervoort et al., 2019). In this study, NCIE-I, NCIE-II, and NCIEs correspond to periods of volcanic activity VA-I, VAI-II, VA-III, and VA-IV, respectively (Fig. 3). This near-synchronous relationship of NCIEs and sedimentary Hg anomalies implies a common source in the baking of organic-rich sediments by intrusive magma, which may have occurred during the initial stages of volcanic intrusion into the organic-rich sink (e.g., Svensen et al., 2004, 2009; Shen et al., 2019, 2022b). This drives a negative $\delta^{13}C$ excursion throughout the exogenic carbon reservoir, including the atmosphere-ocean system, which is then recorded in terrestrial OM (e.g., Shen et al., 2019, 2020). In summary, we consider that sedimentary Hg (and Hg/Al_2O_3) anomalies in this study are a reliable proxy for volcanic activity.

During the Middle Jurassic, global volcanism was associated with the breakup of Pangaea and the rapid spread of the Ligurian and Central Atlantic Oceans (e.g., Dera et al., 2011), with volcanic activity in Patagonia 2 (~172-162 Ma; with a marked peak at 170-168 Ma), North Sea 2 (Bajocian-Oxfordian stages), and northeast Asia (Bathonian-Oxfordian stages; beginning at ~168 Ma with the main eruption phase at 165 ± 2 Ma) (e.g., Pankhurst et al., 2000; Wu et al., 2000, 2001; Dera et al., 2011 and references therein; Huang, 2019). However, it is difficult to distinguish an individual source of the Hg in our study area because of the overlapping eruption ages of these geographically widespread volcanic events (Fig. 9).

Based on the widespread volcanism of the time, and the temporal relationship between Hg (and Hg/Al_2O_3) anomalies, NCIEs, climatic warming, and floral change recorded in this study (Figs. 3, 9), we invoke a scenario in which volcanism was a key driver of change in the Qaidam Basin during the Middle Jurassic. Notably, our results reveal significant differences in the humidity associated with the three volcanically-induced warming events. The first two warming events were accompanied by humid conditions and the occurrence of coal accumulation, but the third warming event was accompanied by dry conditions and the weakening or stagnation of coal accumulation (Figs. 3, 9). This drying event resulted in a decrease in plant diversity and a significant loss of ferns spores in the study area, and a rapid increase in the proportions of *Classopollis* pollen (Fig. 2; Table S1), as seen in other continental strata from the late Middle Jurassic (Vakhrameev, 1991; Deng et al., 2017).

This is because, unlike other plants that produce fern spores and gymnosperm pollen, Cheirolepidiaceae (*Classopollis*) plants are better adapted to turbulent environments and climates (Vakhrameev, 1991; Jin et al., 2022; Zhang et al., 2022).

The intensification of the greenhouse effect and of the potential monsoon circulation in East Asia, as well as the true polar wander, have been proposed as the cause(s) of the dry climates of the late Middle Jurassic (Wang et al., 2005; Yi et al., 2019). The intensification of greenhouse effects and the true polar wander affects global atmospheric circulation and can drive significant changes in the global climate (e.g., Wang et al., 2005; Ma et al., 2018; Yi et al., 2019; Ruhl et al., 2020). Previous studies on the paleomagnetic and geochronological of Jurassic volcanic rocks in North China have shown that the true polar wander led to dry climatic events during the late Middle Jurassic (Yi et al., 2019). Similarly, previous studies of sedimentology, geochemistry, and paleobotany in China have suggested that a rapid increase in the greenhouse effect resulted in a relatively arid climate in the late Middle Jurassic (Wang et al., 2005; Deng et al., 2017), but the cause of this increase in the greenhouse effect has remained a mystery. Based on our data, we suggest that major volcanism was responsible for a rapid increase in global temperatures and the intensification of the greenhouse effect in the Middle Jurassic. It is likely that the different contributing factors acted in tandem to drive the late Middle Jurassic aridification of the study area.

6. Conclusions

(1) Middle Jurassic $\delta^{13}C_{org}$ values in the study area fluctuated significantly and vary from −26.1‰ to −21.0‰ ($\bar{x} = -23.3$‰) and reveal five relatively low-value intervals (heavier plateaus) and four relatively high-value intervals (lighter plateaus). Relatively low values were found in the late Toarcian stage, the Aalenian-Bajocian boundary, the Bajocian-Bathonian boundary, the middle Callovian stage, and the early Oxfordian stage while relatively high values were found in the Aalenian stage, the early Bajocian stage, at the Bathonian-Callovian boundary, and at the Callovian-Oxfordian boundary. Three prominent negative carbon isotope excursions (NCIEs) are identified.

(2) Twenty-seven spore, twenty-six pollen, and five algae genera have been identified and are assigned to six palynological assemblage zones based on the palynomorph abundance variations and CONISS. Biostratigraphy (palynological fossils) and chemostratigraphy ($\delta^{13}C_{org}$ patterns) constrain the strata to the late Early Jurassic Toarcian to early Late Jurassic Oxfordian interval. Based on our palynological study, PCA, H/X ratios, and nMDS, the terrestrial vegetation and climate experienced a change from conifer to fern and back to conifer dominance associated with climatic (arid-humid-arid) changes between the late Early Jurassic and early Late Jurassic.

(3) Volcanism appears to be a key driver of environmental, climatic, and floral changes in the study area. Thus, three NCIEs associated with warming episodes (inferred from palynological fossil and PCA results) have temporal coincidence with Hg (and Hg/Al_2O_3) loading to the system, suggesting that these phenomena have volcanic origins.

Author contributions

PZ, MY, JL, SL, and JH designed the research. JL, PZ, MY, KZ, ZH, LS, JH and DB analyzed the data. PZ, MY, JL, KZ, LS, JH and DB wrote the manuscript. All authors contributed to the interpretation of the data and the final manuscript.

Declaration of Competing Interest

MY was employed by PetroChina. All authors declare that the research was conducted in the absence of any commercial or financial relationships that could be construed as a potential conflict of interest.

Data availability

All data needed to evaluate the conclusions are present in the paper and/or the Supplementary Materials. All palynological slides are housed at the State Key Laboratory of Coal Resources and Safe Mining (Beijing).

Acknowledgments

We are grateful to Suping Peng and Shifeng Dai (China University of Mining and Technology Beijing) for their comments on earlier versions of the manuscript. We also thank Alan Haywood and two anonymous reviewers for constructive and helpful reviews and comments on the manuscript. Financial support was provided by the Open Fund of National Energy Shale Gas Research and Development Centre (2022-KFKT-14), the Major Science and Technology Projects of PetroChina during the 14th Five-Year Plan (2021DJ2303), the National Natural Science Foundation of China (Grant nos. 42172196, 41772161, and 41472131), the Natural Environment Research Council's (NERC) Biosphere Evolution, Transition, and Resilience (BETR) Program (grant NE/P0137224/1), and NERC grant NE/V001639/1.

Appendix A. Supplementary data

Supplementary data to this article can be found online at https://doi.org/10.1016/j.gloplacha.2023.104094.

References

Al-Mojel, A., Dera, G., Razin, P., Le Nindre, Y.M., 2018. Carbon and oxygen isotope stratigraphy of Jurassic platform carbonates from Saudi Arabia: Implications for diagenesis, correlations and global paleoenvironmental changes. Palaeogeogr. Palaeoclimatol. Palaeoecol. 511, 388–402. https://doi.org/10.1016/j.palaeo.2018.09.005.

Balme, B.E., 1995. Fossil in situ spores and pollen grains: an annotated catalogue. Rev. Palaeobot. Palynol. 87, 81–323. https://doi.org/10.1016/0034-6667(95)93235-X.

Bartolini, A., Cecca, F., 1999. 20 my hiatus in the Jurassic of Umbria-Marche Apennines (Italy): carbonate crisis due to eutrophication. Comptes Rendus l'Académie des Sci. – Ser. IIA - Earth Planet. Sci. 329, 587–595. https://doi.org/10.1016/S1251-8050(00)87215-8.

Bartolini, A., Baumgartner, P.O., Guex, J., 1999. Middle and late Jurassic radiolarian palaeoecology versus carbon-isotope stratigraphy. Palaeogeogr. Palaeoclimatol. Palaeoecol. 145, 43–60. https://doi.org/10.1016/S0031-0182(98)00097-2.

Bower, J., Savage, K.S., Weinman, B., Barnett, M.O., Hamilton, W.P., Harper, W.F., 2008. Immobilization of mercury by pyrite (FeS_2). Environ. Pollut. 156, 504–514. https://doi.org/10.1016/j.envpol.2008.01.011.

Cloern, J.E., Canuel, E.A., Harris, D., 2002. Stable carbon and nitrogen isotope composition of aquatic and terrestrial plants of the San Francisco Bay estuarine system. Limnol. Oceanogr. 47, 713–729. https://doi.org/10.4319/lo.2002.47.3.0713.

Couper, R.A., 1958. British Mesozoic microspores and pollen grains. A systematic and stratigraphic study. Palaeontogr. Abteilung B -Stuttgart. 103, 75–179. https://doi.org/10.1117/12.2056904.

Dal Corso, J., Gianolla, P., Rigo, M., Franceschi, M., Roghi, G., Mietto, P., Manfrin, S., Raucsik, B., Budai, T., Jenkyns, H.C., Reymond, C.E., Caggiati, M., Gattolin, G., Breda, A., Merico, A., Preto, N., 2018. Multiple negative carbon-isotope excursions during the Carnian Pluvial Episode (Late Triassic). Earth-Science Rev. 185, 732–750. https://doi.org/10.1016/j.earscirev.2018.07.004.

Deng, S., Lu, Y., Zhao, Y., Fan, R., Wang, Y., Yang, X., Li, X., Sun, B., 2017. The Jurassic palaeoclimate regionalization and evolution of China. Earth Sci. Front. 24, 106–142. https://doi.org/10.13745/j.esf.2017.01.007.

Dera, G., Brigaud, B., Monna, F., Laffont, R., Pucéat, E., Deconinck, J.F., Pellenard, P., Joachimski, M.M., Durlet, C., 2011. Climatic ups and downs in a disturbed Jurassic world. Geology 39, 215–218. https://doi.org/10.1130/G31579.1.

Du, B., 1985. Sporo-pollen assemblages from the Middle Jurassic in the WangJiashan Basin of Jingyuan,Gansu,and their stratigraphic and paleogeographic significance. Geol. Rev. 31, 131–141 https://doi.org/CNKI:SUN:DZLP.0.1985-02-005.

Du, B., Li, X., Duan, W., 1982. Spore-pollen assemblages from Yan'an and Zhiluo formations in Chongxin County, Gansu Province. Acta Palaeontol. Sin. 21, 597–606 https://doi.org/CNKI:SUN:GSWX.0.1982-05-012.

Farrah, H., Pickering, W.F., 1978. The sorption of mercury species by clay minerals. Water Air Soil Pollut. 9, 23–31. https://doi.org/10.1007/BF00185744.

Fielding, C.R., Frank, T.D., McLoughlin, S., Vajda, V., Mays, C., Tevyaw, A.P., Winguth, A., Winguth, C., Nicoll, R.S., Bocking, M., Crowley, J.L., 2019. Age and pattern of the southern high-latitude continental end-Permian extinction constrained by multiproxy analysis. Nat. Commun. 10, 385. https://doi.org/10.1038/s41467-018-07934-z.

Galasso, F., Feist-Burkhardt, S., Schneebeli-Hermann, E., 2022. The palynology of the Toarcian Oceanic Anoxic Event at Dormettingen, Southwest Germany, with emphasis on changes in vegetational dynamics. Rev. Palaeobot. Palynol. 304, 104701 https://doi.org/10.1016/j.revpalbo.2022.104701.

Grasby, S.E., Beauchamp, B., 2009. Latest Permian to early Triassic basin-to-shelf anoxia in the Sverdrup Basin, Arctic Canada. Chem. Geol. 264, 232–246. https://doi.org/10.1016/j.chemgeo.2009.03.009.

Grasby, S.E., Sanei, H., Beauchamp, B., 2011. Catastrophic dispersion of coal fly ash into oceans during the latest Permian extinction. Nat. Geosci. 4, 104–107. https://doi.org/10.1038/ngeo1069.

Grasby, S.E., Beauchamp, B., Bond, D.P.G., Wignall, P., Talavera, C., Galloway, J.M., Piepjohn, K., Reinhardt, L., Blomeier, D., 2015. Progressive environmental deterioration in northwestern Pangea leading to the latest Permian extinction. Geol. Soc. Am. Bull. 127, 1331–1347. https://doi.org/10.1130/B31197.1.

Grasby, S.E., Beauchamp, B., Bond, D.P.G., Wignall, P.B., Sanet, H., 2016. Mercury anomalies associated with three extinction events (Capitanian Crisis, latest Permian Extinction and the Smithian/Spathian Extinction) in NW Pangea. Geol. Mag. 153, 285–297. https://doi.org/10.1017/S0016756815000436.

Grasby, S.E., Them, T.R., Chen, Z., Yin, R., Ardakani, O.H., 2019. Mercury as a proxy for volcanic emissions in the geologic record. Earth Sci. Rev. 196, 102880 https://doi.org/10.1016/j.earscirev.2019.102880.

Grasby, S.E., Liu, X., Yin, R., Ernst, R.E., Chen, Z., 2020. Toxic mercury pulses into late Permian terrestrial and marine environments. Geology 48, 830–833. https://doi.org/10.1130/G47295.1.

Guo, B., Eley, Y., Hilton, J., Zou, M., Wang, Q., 2020. Carbon-isotope, petrological and floral record in coals: Implication for Bajocian (Middle Jurassic) climate change. Int. J. Coal Geol. 220, 103417 https://doi.org/10.1016/j.coal.2020.103417.

Hesselbo, S.P., Morgans-Bell, H.S., McElwain, J.C., Rees, P.M.A., Robinson, S.A., Ross, C. E., 2003. Carbon-cycle perturbation in the Middle Jurassic and accompanying changes in the terrestrial paleoenvironment. J. Geol. 111, 259–276. https://doi.org/10.1086/373968.

Huang, P., 1995. Early-Middle Jurassic sporopollen assemblages from Dananhu Coalfield of Tuha Basin, Xinjiang. Acta Palaeontol. Sin. 34, 171–193 https://doi.org/CNKI:SUN:GSWX.0.1995-02-002.

Huang, P., 2000. Discovery of Middle Jurassic palynogical assemblage from Beixiangshan of Nanjing. Acta Palaeontol. Sin. 17, 457–469. https://doi.org/10.3969/j.issn.1000-0674.2000.04.014.

Huang, D., 2019. Jurassic integrative stratigraphy and timescale of China. Sci. China Earth Sci. 62, 223–255. https://doi.org/10.1007/s11430-017-9268-7.

Huang, P., Li, J., 2007. Sporopollen assemblages from the Xishanyao and Toutunhe formations at the Honggou section of the Manasi river,Xinjiang and their stratigraphical significance. Acta Micropalaeontol. Sin. 24, 170–193 https://doi.org/CNKI:SUN:WSGT.0.2007-02-003.

Jenkyns, H.C., Jones, C.E., GrÖcke, D.R., Hesselbo, S.P., Parkinson, D.N., 2002. Chemostratigraphy of the Jurassic System: applications, limitations and implications for palaeoceanography. J. Geol. Soc. Lond. 159, 351–378. https://doi.org/10.1144/0016-764901-130.

Jin, X., Shi, Z., Baranyi, V., Kemp, D.B., Han, Z., Luo, G., Hu, J., He, F., Chen, L., Preto, N., 2020. The Jenkyns Event (early Toarcian OAE) in the Ordos Basin, North China. Glob. Planet. Chang. 193, 103273 https://doi.org/10.1016/j.gloplacha.2020.103273.

Jin, X., Zhang, F., Baranyi, V., Kemp, D.B., Feng, X., Grasby, S.E., Sun, G., Shi, Z., Chen, W., Dal, J., 2022. Early Jurassic massive release of terrestrial mercury linked to floral crisis. Earth Planet. Sci. Lett. 598, 117842 https://doi.org/10.1016/j.epsl.2022.117842.

Li, W., Shang, Y., 1980. Sporo-pollen assemblages from the Mesozoic Coal Series of Western Hubei. Acta Palaeontol. Sin. 19, 201–219.

Li, W., Zhang, X., Feng, Q., Jiao, K., Chen, Y., Zou, K., Cui, H., 2020. Paleoenvironment changes inferred from the analysis of organic elements and carbon isotope characteristics of Jurassic argillaceous rocks in the Dameigou, North Qaidam Basin. Geol. J. China Univ. 26, 704–711. https://doi.org/10.16108/j.issn1006-7493.2019085.

Lindström, S., 2021. Two-phased mass rarity and extinction in land plants during the end-Triassic climate crisis. Front. Earth Sci. 9 https://doi.org/10.3389/feart.2021.780343.

Litwin, R.J., Traverse, A., 1989. Basic guidelines for palynomorph extraction and preparation from sedimentary rocks. Paleontol. Soc. Spec. Publ. 4, 87–98. https://doi.org/10.1017/S2475262200005025.

Liu, Z., 1982. Early and Middle Jurassic sporo-pollen assemblage from the Shiguai Coalfeild of Baotou, Nei Mongol. Acta Palaeontol. Sin. 21, 371–379.

Liu, Z., 1986a. Early and Middle Jurassic sporo-pollen assemblage from the Datong Coalfied of Shanxi, North China. In: Acta Palaeobotaniea, Palynologica, Sinica, 1. Jiangsu Science and Technology Publishing House, Nanjing, pp. 85–124.

Liu, Z., 1986b. In: Nanjing (Ed.), Early and Middle Jurassic sporo-pollen assemblage from the Datong Coalfied of Shanxi, North China. Acta Palaeobotanica, Palynologica, Sinica, 1. Jiangsu Science and Technology Publishing House, pp. 85–124 https://doi.org/ir.nigpas.ac.cn/handle/332004/6248.

Liu, Z., 1990. Spore-pollen assembalge from middle Jurassic Xishanyao Formation of Shawan, Xinjiang, China. Acta Palaeontol. Sin. 29, 63–82 https://doi.org/CNKI:SUN:GSWX.0.1990-01-005.

Liu, Z., 1993. Jurassic sporopollen assemblages from the Beishan coalfield, Qitai, Xinjiang. Acta Micropalaeontol. Sin. 10, 13–36 https://doi.org/CNKI:SUN:WSGT.0.1993-01-001.

Liu, Z., Sun, G., 1992. Early and Middle Jurassic sporo-pollen assemblage from Wenquan Coalfield of Xinjiang, China and their stratigraphical significance. Acta Palaeontol. Sin. 31, 629–645 https://doi.org/CNKI:SUN:GSWX.0.1992-06-000.

Liu, T., Shao, L., Cao, D., Ju, Q., Guo, J., Lu, J., 2013. Jurassic Coal Resources Formation Conditions and Resource Evaluation in the Northern Margin of Qaidam Basin. Geological Publishing House, Beijing.

Lu, J., Shao, L., Liu, T., Wen, H., Wang, H., Shang, L., Yang, M., 2007. A sequence stratigraphic analysis of the Jurassic coal measures in Yuqia region of Northern Qaidam basin. Coal Geol. Explor. 35, 1–6 https://doi.org/CNKI:SUN:MDKT.0.2007-01-000.

Lu, J., Shao, L., Wang, Z., Li, Y., Wang, S., 2014a. Organic carbon isotope composition and paleoclimatic evolution of Jurassic coal seam in the northern Qaidam basin. J. China Univ. Min. Technol. 43, 612–618. https://doi.org/10.13247/j.cnki.jcumt.000091.

Lu, J., Shao, L., Yang, M., Li, Y., Zhang, Z., Wang, S., Yun, Q., 2014b. Coal facies evolution,sequence stratigraphy and palaeoenvironment of swamp in terrestrial basin. J. China Coal Soc. 39, 2473–2481. https://doi.org/10.13225/j.cnki.jccs.2013.1779.

Lu, J., Yang, M., Shao, L., Chen, S., Li, Y., Zhou, K., Wang, W., 2016. Paleoclimate change and sedimentary environment evolution,coal accumulation: a Middle Jurassic terrestrial. J. China Coal Soc. 41, 1788–1797. https://doi.org/10.13225/j.cnki.jccs.2016.0061.

Lu, J., Yang, M., Sun, X., Shao, L., Zhang, F., 2018. Jurassic coal maceral and deposition rate of peat in the northern Qaidam Basin. J. Min. Sci. Technol. 3, 1–8. https://doi.org/10.19606/j.cnki.jmst.2018.01.001.

Lu, J., Zhang, P., Yang, M., Shao, L., Hilton, J., 2020a. Continental records of organic carbon isotopic composition ($\delta^{13}C_{org}$), weathering, paleoclimate and wildfire linked to the End-Permian Mass Extinction. Chem. Geol. 558, 119764 https://doi.org/10.1016/j.chemgeo.2020.119764.

Lu, J., Zhou, K., Yang, M., Eley, Y., Shao, L., Hilton, J., 2020b. Terrestrial organic carbon isotopic composition ($\delta^{13}C_{org}$) and environmental perturbations linked to early Jurassic volcanism: evidence from the Qinghai-Tibet Plateau of China. Glob. Planet. Chang. 195, 103331 https://doi.org/10.1016/j.gloplacha.2020.103331.

Lu, J., Zhou, K., Yang, M., Shao, L., 2020c. Jurassic continental coal accumulation linked to changes in palaeoclimate and tectonics in a fault-depression superimposed basin, Qaidam Basin, NW China. Geol. J. 55, 7998–8016. https://doi.org/10.1002/gj.3921.

Lu, J., Zhang, P., Dal Corso, J., Yang, M., Wignall, P.B., Greene, S.E., Shao, L., Lyu, D., Hilton, J., 2021a. Volcanically driven lacustrine ecosystem changes during the Carnian Pluvial Episode (Late Triassic). Proc. Natl. Acad. Sci. U. S. A. 118, e2109895118 https://doi.org/10.1073/pnas.2109895118.

Lu, J., Zhou, K., Yang, M., Zhang, P., Shao, L., Hilton, J., 2021b. Records of organic carbon isotopic composition ($\delta^{13}C_{org}$) and volcanism linked to changes in atmospheric $p\mathrm{CO}_2$ and climate during the late Paleozoic Icehouse. Glob. Planet. Chang. 207, 103654 https://doi.org/10.1016/j.gloplacha.2021.103654.

Ma, J., Chadwick, R., Seo, K.-H., Dong, C., Huang, G., Foltz, G.R., Jiang, J.H., 2018. Responses of the tropical atmospheric circulation to climate change and connection to the hydrological cycle. Annu. Rev. Earth Planet. Sci. 46, 549–580. https://doi.org/10.1146/annurev-earth-082517-010102.

Marchetti, L., Forte, G., Kustatscher, E., DiMichele, W.A., Lucas, S.G., Roghi, G., Juncal, M.A., Hartkopf-Fröder, C., Krainer, K., Morelli, C., Ronchi, A., 2022. The Artinskian Warming Event: an Euramerican change in climate and the terrestrial biota during the early Permian. Earth-Science Rev. 226, 103922 https://doi.org/10.1016/j.earscirev.2022.103922.

Mays, C., Vajda, V., Frank, T.D., Fielding, C.R., Nicoll, R.S., Tevyaw, A.P., McLoughlin, S., 2020. Refined Permian–Triassic floristic timeline reveals early collapse and delayed recovery of south polar terrestrial ecosystems. GSA Bull. 132, 1489–1513. https://doi.org/10.1130/B35355.1.

Mays, C., McLoughlin, S., Frank, T.D., Fielding, C.R., Slater, S.M., Vajda, V., 2021. Lethal microbial blooms delayed freshwater ecosystem recovery following the end-Permian extinction. Nat. Commun. 12 https://doi.org/10.1038/s41467-021-25711-3.

Meng, F., 1999. Middle Jurassic fossil plants in the Yangtze gorges area of China and their paleo-climatic environment. Geol. Miner. Resour. South China 3, 19–27 https://doi.org/CNKI:SUN:HNKC.0.1999-03-002.

Mueller, S., Hounslow, M.W., Kürschner, W.M., 2016a. Integrated stratigraphy and palaeoclimate history of the Carnian Pluvial event in the Boreal realm; new data from the upper triassic kapp Toscana group in Central Spitsbergen (Norway). J. Geol. Soc. Lond. 173, 186–202. https://doi.org/10.1144/jgs2015-028.

Mueller, S., Krystyn, L., Kürschner, W.M., 2016b. Climate variability during the Carnian Pluvial phase — a quantitative palynological study of the Carnian sedimentary succession at Lunz am See, Northern Calcareous Alps, Austria. Palaeogeogr. Palaeoclimatol. Palaeoecol. 441, 198–211. https://doi.org/10.1016/j.palaeo.2015.06.008.

Na, Y., Manchester, S.R., Sun, C., Zhang, S., 2015. The Middle Jurassic palynology of the Daohugou area, Inner Mongolia, China, and its implications for palaeobiology and palaeogeography. Palynology 39, 270–287. https://doi.org/10.1080/01916122.2014.961664.

O'Dogherty, L., Sandoval, J., Bartolini, A., Bruchez, S., Bill, M., Guex, J., 2006. Carbon-isotope stratigraphy and ammonite faunal turnover for the Middle Jurassic in the Southern Iberian palaeomargin. Palaeogeogr. Palaeoclimatol. Palaeoecol. 239, 311–333. https://doi.org/10.1016/j.palaeo.2006.01.018.

Oehlert, A.M., Swart, P.K., 2014. Interpreting carbonate and organic carbon isotope covariance in the sedimentary record. Nat. Commun. 5, 4672. https://doi.org/10.1038/ncomms5672.

Pankhurst, R.J., Riley, T.R., Fanning, C.M., Kelley, S.P., 2000. Episodic silicic volcanism in Patagonia and the Antarctic Peninsula: chronology of magmatism associated with the break-up of Gondwana. J. Petrol. 41, 605–625. https://doi.org/10.1093/petrology/41.5.605.

Pellenard, P., Tramoy, R., Pucéat, E., Huret, E., Martinez, M., Bruneau, L., Thierry, J., 2014. Carbon cycle and sea-water palaeotemperature evolution at the Middle-Late Jurassic transition, eastern Paris Basin (France). Mar. Pet. Geol. 53, 30–43. https://doi.org/10.1016/j.marpetgeo.2013.07.002.

Pocock, S.A.J., 1970. Palynology of the jurassic sediments of Western Canada. Part 1. (continued) Terrestrial species. Palaeontogr. Abt. B 130, 73–136.

Pu, R., Wu, H., 1982. Sporo-pollen from the Late Mesozoic beds in eastern Heilongjiang Province. Bull. Shenyang Inst. Geol. Miner. Resour. Acad. Geol. Sci. 383–456.

Pyle, D.M., Mather, T.A., 2003. The importance of volcanic emissions for the global atmospheric mercury cycle. Atmos. Environ. 37, 5115–5124. https://doi.org/10.1016/j.atmosenv.2003.07.011.

Ravichandran, M., 2004. Interactions between mercury and dissolved organic matter—a review. Chemosphere 55, 319–331. https://doi.org/10.1016/j.chemosphere.2003.11.011.

Rostovtseva, J.I., 2011. New palynological data about middle Jurassic sediments in Northwest Moscow. Mosc. Univ. Geol. Bull. 66, 348–353. https://doi.org/10.3103/s0145875211050097.

Ruhl, M., Hesselbo, S.P., Al-Suwaidi, A., Jenkyns, H.C., Damborenea, S.E., Manceñido, M.O., Storm, M., Mather, T.A., Riccardi, A.C., 2020. On the onset of Central Atlantic Magmatic Province (CAMP) volcanism and environmental and carbon-cycle change at the Triassic–Jurassic transition (Neuquén Basin, Argentina). Earth-Science Rev. 208, 103229 https://doi.org/10.1016/j.earscirev.2020.103229.

Saltzman, M.R., Thomas, E., 2012. Carbon isotope stratigraphy. In: The Geologic Time Scale. Elsevier, pp. 207–232. https://doi.org/10.1016/B978-0-444-59425-9.00011-1.

Sanei, H., Grasby, S.E., Beauchamp, B., 2012. Latest Permian mercury anomalies. Geology 40, 63–66. https://doi.org/10.1130/G32596.1.

Schlaich, M., Aigner, T., 2017. Facies and integrated sequence stratigraphy of an Epeiric Carbonate Ramp Succession: Dhruma formation, Sultanate of Oman. Depos. Rec. 3, 92–132. https://doi.org/10.1002/dep2.28.

Schouten, S., Woltering, M., Rijpstra, I., Sluijs, A., Brinkhuis, H., Sinninghe-Damste, J., 2007. The Paleocene–Eocene carbon isotope excursion in higher plant organic matter: differential fractionation of angiosperms and conifers in the Arctic. Earth Planet. Sci. Lett. 258, 581–592. https://doi.org/10.1016/j.epsl.2007.04.024.

Shang, Y., 1997. Middle jurassic palynology of carapace Nunatak, Victoria Land, Antarctica. Acta Palaeontol. Sin. 36, 170–186. https://doi.org/10.1088/0256-307X/13/12/010.

Shao, L., Li, M., Li, Y., Zhang, Y., Lu, J., Zhang, W., Tian, Z., Wen, H., 2014. Geological characteristics and controlling factors of shale gas in the Jurassic of the northern Qaidam Basin. Earth Sci. Front. 21, 311–322. https://doi.org/10.13745/j.esf.2014.04.031.

Shen, J., Yu, J., Chen, J., Algeo, T.J., Xu, G., Feng, Q., Shi, X., Planavsky, N.J., Shu, W., Xie, S., 2019. Mercury evidence of intense volcanic effects on land during the Permian-Triassic transition. Geology 47, 1117–1121. https://doi.org/10.1130/G46679.1.

Shen, J., Feng, Q., Algeo, T.J., Liu, Jinling, Zhou, C., Wei, W., Liu, Jiangsi, Them, T.R., Gill, B.C., Chen, J., 2020. Sedimentary host phases of mercury (Hg) and implications for use of Hg as a volcanic proxy. Earth Planet. Sci. Lett. 543, 116333 https://doi.org/10.1016/j.epsl.2020.116333.

Shen, J., Yin, R., Zhang, S., Algeo, T.J., Bottjer, D.J., Yu, J., Xu, G., Penman, D., Wang, Y., Li, L., Shi, X., Planavsky, N.J., Feng, Q., Xie, S., 2022a. Intensified continental chemical weathering and carbon-cycle perturbations linked to volcanism during the Triassic–Jurassic transition. Nat. Commun. 13, 299. https://doi.org/10.1038/s41467-022-27965-x.

Shen, J., Yin, R., Algeo, T.J., Svensen, H.H., Schoepfer, S.D., 2022b. Mercury evidence for combustion of organic-rich sediments during the end-Triassic crisis. Nat. Commun. 13, 1307. https://doi.org/10.1038/s41467-022-28891-8.

Sun, F., 1989. Early and Middle Jurassic sporo-pollen assemblages of Qiquanhu Coalfield of Turfan, Xinjiang. Acta Bot. Sin. 31, 368–646 https://doi.org/CNKI:SUN:ZWXB.0.1989-08-011.

Svensen, H., Planke, S., Malthe-Sørenssen, A., Jamtveit, B., Myklebust, R., Rasmussen Eidem, T., Rey, S.S., 2004. Release of methane from a volcanic basin as a mechanism for initial Eocene global warming. Nature 429, 542–545. https://doi.org/10.1038/nature02566.

Svensen, H., Planke, S., Polozov, A.G., Schmidbauer, N., Corfu, F., Podladchikov, Y.Y., Jamtveit, B., 2009. Siberian gas venting and the end-Permian environmental crisis. Earth Planet. Sci. Lett. 277, 490–500. https://doi.org/10.1016/j.epsl.2008.11.015.

Them, T.R., Jagoe, C.H., Caruthers, A.H., Gill, B.C., Grasby, S.E., Gröcke, D.R., Yin, R., Owens, J.D., 2019. Terrestrial sources as the primary delivery mechanism of mercury to the oceans across the Toarcian Oceanic Anoxic Event (Early Jurassic). Earth Planet. Sci. Lett. 507, 62–72. https://doi.org/10.1016/j.epsl.2018.11.029.

Traverse, A.T., 2007. Topics in Geobiology, Paleopalynology. Springer, pp. 1–581.

Vakhrameev, V.A., 1991. Jurassic and Cretaceous Floras and Climates of the Earth. Cambridge University Press.

Vakhrameyev, V.A., 1982. Classopollis pollen as an indicator of Jurassic and cretaceous climate. Int. Geol. Rev. 24, 1190–1196. https://doi.org/10.1080/00206818209451058.

Van Konijnenburg-Van Cittert, J.H.A., 1978. Osmundaceous spores in situ from the Jurassic of Yorkshire, England. Rev. Palaeobot. Palynol. 26, 125–141. https://doi.org/10.1016/0034-6667(78)90009-X.

Vervoort, P., Adloff, M., Greene, S.E., Kirtland Turner, S., 2019. Negative carbon isotope excursions: an interpretive framework. Environ. Res. Lett. 14, 085014 https://doi.org/10.1088/1748-9326/ab3318.

Wang, C., Tong, G., 1982. Notes on some Middle Jurassic pollen and spores from Fengxian, Jiangsu. In: Palynological Society of China (Ed.), Selected Papers from the First Symposium of the Palynological Society of China (1979). Science Press, Beijing, pp. 100–104 (in Chinese).

Wang, Y., Jiang, D., Yang, H., Sun, F., 1998. Middle Jurassic Spore-pollen Assemblages from Turpan-Shanshan Area, Xinjiang. Acta Bot. Sin. 40, 969–976.

Wang, Y., Mosbrugger, V., Zhang, H., 2005. Early to Middle Jurassic vegetation and climatic events in the Qaidam Basin, Northwest China. Palaeogeogr. Palaeoclimatol. Palaeoecol. 224, 200–216. https://doi.org/10.1016/j.palaeo.2005.03.035.

Wang, P., Zhang, P., Yang, Z., Dong, X., Ning, K., Zhou, Q., 2021. Quaternary stratigraphy and paleoenvironmental evolution of the Ningbo Coastal Plain revealed by core Z02. Chin. J. Appl. Ecol. 32, 453–466. https://doi.org/10.13287/j.1001-9332.202102.009.

Wei, B., 2000. An analysis on tectonic paleogeography of the Qaidam Bsain, NW China. Earth Sci. Front. 7, 421–429. https://doi.org/10.3321/j.issn:1005-2321.2000.04.009.

Wellman, C.H., Osterloff, P.L., Mohiuddin, U., 2003. Fragments of the earliest land plants. Nature 425, 282–285. https://doi.org/10.1038/nature01884.

Wignall, P.B., Atkinson, J.W., 2020. A two-phase end-Triassic mass extinction. Earth-Science Rev. 208, 103282 https://doi.org/10.1016/j.earscirev.2020.103282.

Wu, F.Y., Sun, D.Y., Li, H.M., Wang, X.L., 2000. Zircon U-Pb ages for the basement rocks of the Songliao Basin. Chin. Sci. Bull. 45, 656–660. https://doi.org/10.3321/j.issn:0023-074X.2000.06.021.

Wu, F.Y., Sun, D.Y., Li, H.M., Wang, X.L., 2001. The nature of basement beneath the Songliao Basin in NE China: geochemical and isotopic constraints. Phys. Chem. Earth, Part A Solid Earth Geod. 26, 793–803. https://doi.org/10.1016/S1464-1895(01)00128-4.

Wu, Y., Chu, D., Tong, J., Song, H.J., Dal Corso, J., Wignall, P.B., Song, H.Y., Du, Y., Cui, Y., 2021. Six-fold increase of atmospheric pCO2 during the Permian–Triassic mass extinction. Nat. Commun. 12, 2137. https://doi.org/10.1038/s41467-021-22298-7.

Xu, Y., Zhang, W., 1980. Jurassic spores and pollen grains. In: Institute of Geology, Chinese Academy of Geological Sciences (Ed.), The Mesozoic Stratigraphy and Palaeontology in the Ordos Basin, vol. 1. Geological Publishing House, Beijing.

Xu, X., Shao, L., Eriksson, K.A., Pang, B., Wang, S., Yang, C., Hou, H., 2022. Terrestrial records of the early Albian Ocean Anoxic Event: evidence from the Fuxin lacustrine basin, NE China. Geosci. Front. 13, 101275 https://doi.org/10.1016/j.gsf.2021.101275.

Yan, C., Yuan, J., Cheng, Q., 2007. Palynofacies and Oil potential of lower-middle Jurassic in the east part of northern Qaidam basin. Adv. Earth Science 22, 1268–1273.

Yang, P., Xie, Z., Yuan, X., Zhu, S., Yi, D., 2006. Palaeoecological characteristics and its palaeogeographic significance of the Jurassic in northern margin of Qaidam Basin. J. Palaeogeogr. 8, 165–173. https://doi.org/10.3969/j.issn.1671-1505.2006.02.003.

Yang, Y., Guo, Z., Luo, Y., 2017. Middle-late Jurassic tectonostratigraphic evolution of Central Asia, implications for the collision of the Karakoram-Lhasa Block with Asia. Earth-Science Rev. 166, 83–110. https://doi.org/10.1016/j.earscirev.2017.01.005.

Yi, Z., Liu, Y., Meert, J.G., 2019. A true polar wander trigger for the great jurassic East Asian aridification. Geology 47, 1112–1116. https://doi.org/10.1130/G46641.1.

Yu, L., Xiao, A., Wu, L., Tian, Y., Rittner, M., Lou, Q., Pan, X., 2017. Provenance evolution of the Jurassic northern Qaidam Basin (West China) and its geological implications: evidence from detrital zircon geochronology. Int. J. Earth Sci. 106, 2713–2726. https://doi.org/10.1007/s00531-017-1455-z.

Zhang, W., 1987. Jurassic Spores and Pollen Grains. Biostratigraphy of the Yangtze Gorge Area (4) Triassic and Jurassic. Geological Publishing House, Beijing.

Zhang, W., 1989. Jurassic sporo-pollen assemblages from some parts of eastern China. In: The stratigraphical Group of Institute of Geology, Chinese Academy of Geological Sciences (Ed.), Tectonic-Magmatic Evolution and Metallogeny of Eastern China, 2. The Palaeontology and str. Geological Publishing House, Beijing.

Zhang, W., 1990. Jurassic sporo-pollen assemblages in Junggar Basin of Xinjiang. In: Institute of Geology, Chinese Academy of Geological Sciences, Research Institute of Petrole— um Exploration and Development, Xinjiang Petroleum Administration (Ed.), Permian to Tertiary Strata. China Environment Science Press, Beijing.

Zhang, H., 1998. Jurassic Coal-bearing Strata and Coal Accumulation Pattern in Northwestern China. Geological Publishing House, Beijing. https://doi.org/10.3969/j.issn.1001-1986.2018.06.003.

Zhang, P., Lu, J., Yang, M., Bond, D.P.G., Greene, S.E., Liu, L., Zhang, Y., Wang, Y., Wang, Z., Li, S., Shao, L., Hilton, J., 2022. Volcanically-induced environmental and floral changes across the Triassic-Jurassic (T-J) transition. Front. Ecol. Evol. 10, 853404 https://doi.org/10.3389/fevo.2022.853404.

Zhang, P., Yang, M., Lu, J., Bond, D.P.G., Zhou, K., Xu, X., Wang, Y., He, Z., Bian, X., Shao, L., Hilton, J., 2023. End-Permian terrestrial ecosystem collapse in North China: evidence from palynology and geochemistry. Glob. Planet. Chang. 222, 104070 https://doi.org/10.1016/j.gloplacha.2023.104070.

Zhao, Z., Zhang, X., Li, X., Sun, Z., Zeng, J., Wang, Y., 2019. The discovery of the sporopollen fossils from the Middle Jurassic Yangye Formation in Qiemo area of Xinjiang and its geological significance. Geol. Bull. China 38, 1603–1614 https://doi.org/CNKI:SUN:ZQYD.0.2019-10-003.

Zhou, K., Lu, J., Zhang, S., Yang, M., Gao, R., Shao, L., Hilton, J., 2022. Volcanism driven Pliensbachian (early Jurassic) terrestrial climate and environment perturbations. Glob. Planet. Chang. 216, 103919 https://doi.org/10.1016/j.gloplacha.2022.103919.